Cell

Transcriptional atlas of intestinal immune cells reveals that neuropeptide α-CGRP orchestrates ILC2 responses

--Manuscript Draft--

Manuscript Number:	CELL-D-19-00257
Full Title:	Transcriptional atlas of intestinal immune cells reveals that neuropeptide α-CGRP orchestrates ILC2 responses
Article Type:	Research Article
Keywords:	
Order of Authors:	Heping Xu
	Jiarui Ding
	Caroline Porter
	Antonia Wallrapp
	Marcin Tabaka
	Sai Ma
	Chienwen Su
	Danielle Dionne
	Lan T. Nguyen
	Ariel Lefkovith
	Orr Ashenberg
	Patrick R. Burkett
	Hai Ning Shi
	Orit Rozenblatt-Rosen
	Daniel B. Graham
	Vijay K. Kuchroo
	Aviv Regev
	Ramnik Xavier, MD
Abstract:	Immune signaling abnormalities in the small intestine can trigger chronic type 2 inflammation. To characterize this response, we analyzed 58,067 immune cells from the mouse small intestine by single-cell RNA-seq at steady state and after induction of a type 2 inflammatory reaction to ovalbumin. Cell type composition and cell programs shifted in response to inflammation, especially in ILC2s. A key transcript in the inflammation-induced program in intestinal KLRG1+ ILC2s was exon 5 of Calca, encoding the alpha-calcitonin gene-related peptide (α-CGRP). α-CGRP antagonized IL-25-induced activation of intestinal ILC2s and reduced their frequency in an ovalbumin reaction model. α-CGRP activated a cAMP response, which suppressed ILC2 proliferation. In homeostasis, α-CGRP was expressed by two subsets of ChAT+ enteric neurons, and genetic perturbation of α-CGRP increased the proportion of intestinal ILC2s and of Tuft cells. Our work supports a model where α-CGRP-mediated neuronal signaling suppresses ILC2 expansion and maintains type 2 immunity homeostasis.

Transcriptional atlas of intestinal immune cells reveals that neuropeptide α-CGRP orchestrates ILC2 responses

Heping Xu,[1,2,10] Jiarui Ding,[1,10] Caroline Porter,[1] Antonia Wallrapp,[3] Marcin Tabaka,[1] Sai Ma,[1] Chienwen Su,[4] Danielle Dionne,[1] Lan T. Nguyen,[1] Ariel Lefkovith,[5] Orr Ashenberg,[1] Patrick R. Burkett,[3] Hai Ning Shi,[4] Orit Rozenblatt-Rosen,[1] Daniel B. Graham,[2,5,6,7] Vijay K. Kuchroo,[1,3] Aviv Regev,[1,8,11*] Ramnik J. Xavier[2,5,6,7,9,12*]

[1]Klarman Cell Observatory, Broad Institute of MIT and Harvard, Cambridge, MA, USA
[2]Department of Molecular Biology, Massachusetts General Hospital, Harvard Medical School, Boston, MA, USA.
[3]Evergrande Center for Immunologic Diseases, Harvard Medical School and Brigham and Women's Hospital, Boston, Massachusetts, USA.
[4]Mucosal Immunology and Biology Research Center, Massachusetts General Hospital and Harvard Medical School, Charlestown, MA, USA
[5]Broad Institute of MIT and Harvard, Cambridge, MA, USA
[6]Gastrointestinal Unit and Center for the Study of Inflammatory Bowel Disease, Massachusetts General Hospital, Harvard Medical School, Boston, MA, USA.
[7]Center for Microbiome Informatics and Therapeutics, Massachusetts Institute of Technology, Cambridge, MA, USA.
[8]Howard Hughes Medical Institute and Koch Institute for Integrative Cancer Research, Department of Biology, Massachusetts Institute of Technology, Cambridge, MA, USA.
[9]Center for Computational and Integrative Biology, Massachusetts General Hospital, Harvard Medical School, Boston, MA, USA.
[10]These authors contributed equally
[11]Senior author
[12]Lead Contact

*Correspondence: xavier@molbio.mgh.harvard.edu (R.J.X.), aregev@broadinstitute.org (A.R.)

SUMMARY

Signaling abnormalities in immune responses in the small intestine can trigger chronic type 2 inflammation, involving interaction of multiple immune cell types. To systematically characterize this response, we analyzed 58,067 immune cells from the mouse small intestine by single-cell RNA-seq (scRNA-seq) at steady state and after induction of a type 2 inflammatory reaction to ovalbumin (OVA). Analysis revealed broad shifts in both cell type composition and cell programs in response to the inflammation, especially in ILC2s. Among the key transcripts associated with an inflammation-induced program in intestinal KLRG1$^+$ ILC2s was exon 5 of *Calca*, which encodes the alpha-calcitonin gene-related peptide (α-CGRP). α-CGRP antagonized IL-25-induced activation of intestinal KLRG1$^+$ ILC2s and reduced ILC2 frequency in an OVA reaction model. α-CGRP activated a cyclic AMP (cAMP) response, which suppressed ILC2 proliferation. In homeostasis, α-CGRP was predominantly expressed by two subsets of ChAT$^+$ enteric neurons, and genetic perturbation of α-CGRP increased the proportion of intestinal KLRG1$^+$ ILC2s and the number of Tuft cells. Our work highlights a model where α-CGRP-mediated neuronal signaling is critical for suppressing ILC2 expansion and maintaining homeostasis of the type 2 immune machinery.

INTRODUCTION

The immune system in the small intestine is comprised of a complex network of innate and adaptive components that sense and respond antigens from the diet, commensal microbiota and pathogens. Dysregulated immune reactions often lead to chronic inflammatory responses, including type 2 inflammation (Gieseck et al., 2018; Hammad and Lambrecht, 2015; Pulendran and Artis, 2012), which in turn plays a key underlying role in several unrelenting inflammatory diseases, including food allergy (Locksley, 2010; Tordesillas et al., 2017).

Type 2 inflammation is characterized by the production of the cytokines interleukin-4 (IL-4), IL-5, IL-13 and IgE antibody, and tightly regulated and coordinated responses across cell types, including T helper 2 (Th2) cells, B cells, dendritic cells (DCs) and mast cells. In particular, ILC2s have emerged as key regulators of tissue homeostasis and type 2 inflammation (Artis and Spits, 2015; Kotas and Locksley, 2018), and form the prominent source of type 2 cytokines at its early stages (Molofsky et al., 2015; Neill et al., 2010; Price et al., 2010). While the core transcriptional program of ILCs maintains their cellular identity and homeostatic type 2 cytokine competency (Ricardo-Gonzalez et al., 2018), their activity in the intestines is shaped by tissue-specific signals, including activation by IL-25 produced by Tuft cells (von Moltke et al., 2016), and suppression by micronutrients (Spencer et al., 2014).

Despite these substantial advances, our understanding of cellular participants in type 2 inflammation, the mechanisms that maintain homeostasis and induce inflammation, and which additional cell types, besides immune cells, may participate in this cellular circuit in the small intestines is incomplete. Single-cell RNA-seq (scRNA-seq) can dissect cellular diversity on a large scale (Tanay and Regev, 2017; Wagner et al., 2016), and identify cell states of individual cell types in response to different stimuli (Bielecki et al., 2018; Haber et al., 2017). For example, scRNA-seq of lung ILCs recently revealed that neuronal-derived Neuromedin U

(NMU) amplifies ILC2 activity in allergic inflammation (Wallrapp et al., 2017), and the same neuron-immune circuit was also shown to induce activation of ILC2s in the small intestine (Cardoso et al., 2017; Klose et al., 2017).

Here, we combine scRNA-seq with physiological and genetic perturbations to dissect the cellular circuit of type 2 intestinal inflammation. To uncover key responding cellular components, we profiled individual immune cells in the lamina propria (LP) and Peyer's patches (PPs), regions of the small intestine enriched for immune cells, in homeostasis and in an intestinal type 2 inflammatory model. Computational analysis showed that both cell compositions and cell programs shifted in response to inflammation, and highlighting in particular the prominent induction of α-CGRP transcription in ILC2s. In inflammatory conditions, α-CGRP suppressed activation of ILC2s, but induced IL-5 expression. α-CGRP stimulation alone *in vitro* induced the expression of a cAMP-response gene module and suppressed cell proliferation. At homeostasis *in vivo*, $ChAT^{+}$ enteric neurons were the predominant source of α-CGRP and constitutively interacted with ILC2s, and genetic perturbation of α-CGRP increased the proportion of intestinal $KLRG1^{+}$ ILC2s and the number of Tuft cells. Our study reveals a neuro-immune cellular circuit that modulates type 2 inflammation, highlighting critical functions of α-CGRP-mediated neuronal signaling in maintaining homeostasis of ILC2s and the type 2 immune machinery.

RESULTS

An atlas of mouse small intestinal immune cells at homeostasis and in type 2 inflammation

To comprehensively characterize small intestinal immune cells, we generated scRNA-Seq profiles for 58,067 immune cells collected from lamina propria (LP) and Peyer's patch (PP) regions at steady state and after induction of a type 2 inflammatory reaction to ovalbumin

(OVA) (Brandt et al., 2003) (**Figure 1A** and **S1A**). To ensure sufficient representation of rare cells, we combined a normalization strategy — removing by flow sorting either a portion of IgD^+ naïve B cells, which are the most abundant cell type in PPs, or all $CD19^+$ B and $CD3^+$ T cells (**Figure S1B, STAR Methods**) — with profiling of a sufficiently large number of cells number ($P>0.99$ to recover at least 15 cells from each cluster, **STAR Methods**) by massively parallel scRNA-seq (Haber et al., 2017) (**STAR Methods**). We obtained 36,797 and 21,270 high quality cells passing initial filtering (**STAR Methods**) from PP and LP regions, respectively.

Overall, we annotated 27 cell subsets across the two compartments, spanning T cells, B cells, ILCs, dendritic cells (DCs), myeloid cells and stromal cells, in frequencies ranging from 0.07% to 14%. Briefly, we first partitioned the cells from the PP regions by unsupervised clustering (**STAR Methods**) into 46 clusters, retained the 97% of cells that were robustly assigned cell identities in each cluster (**STAR Methods**), assigned the cells from the LP regions to the 46 clusters using a classifier (**STAR Methods**), and visualized the data with scvis (Ding et al., 2018), a deep generative model-based method (**Figure 1B** and **S1C, STAR Methods**). Next, we identified genes that were differentially expressed between the cells in each cluster and the remaining cells (**Table S1**, **Methods**), as well as between pairs of clusters (**Table S2**), to elucidate identities of similar cell types/states. We excluded from downstream analysis clusters mostly consisting of contaminants from epithelium, likely doublets, or cells with a small number of Unique Molecular Identifiers (UMIs) (**Figure 1C and S1D**), or lacking distinct markers (**STAR Methods**). Altogether, we retained 27 clusters spanning 85% of the cells and each associated with distinct marker genes (**Figure S1E**, **STAR Methods**).

Importantly, known distinct cell types with highly similar expression profiles were correctly distinguished by our analysis. For example, $NKp46^+$ ILC3s and $CCR6^+$ lymphoid tissue

inducer (LTi) cells were recovered as separate clusters, even though they both require RORγt-controlled expression programs for their fate determination (Robinette et al., 2015). Nevertheless, LTi cells were distinguished by significantly higher expression levels of MHC-II antigen presentation modules (**Figure S1F,** adjusted $P < 0.05$, likelihood ratio test), whose expression on ILCs has been shown to regulate intestinal homeostasis (Hepworth et al., 2013).

The atlas highlighted expected differences in cellular composition between the LP and PP regions (**Figure 1D** and **S1G**). For example, resting and $IgD^{-}GL7^{+}$ germinal center (GC) B cells were exclusively found in PPs (**Figure S1G**). Conversely, although $CD138^{+}$ antibody-producing plasma cells differentiate from GC B cells, they were predominantly found in LP samples (**Figure S1G**) and confirmed in LP regions *in situ* (**Figure S1H**), highlighting their potential requirement for antibody secretion adjacent to microbes and other antigens in the intestinal mucosa. In another example, LTi cells were significantly enriched (adjusted $P = 4.75*10^{-3}$, Wald test) in PP *vs*. LP regions (**Figure 1D**), which we confirmed by flow cytometry (**Figure 1E,** $P<0.001$, Fisher's exact test). The LTi cell distribution is consistent with their critical function in supporting lymphoid tissue development. ILC1s and Natural Killer (NK) cells were also significantly enriched in PP regions (**Figure 1D,** adjusted $P = 4.29*10^{-7}$ and $P = 1.19*10^{-17}$, respectively, Wald test), suggesting they have unique functions in PPs. Indeed, NK cells suppress affinity maturation of GC B cells (Rydyznski et al., 2018), which probably requires their localization in B cell follicles.

Increase in ILC2 proportions and changes in their expression programs are prominent features of OVA-induced type 2 inflammation

Cell composition was remodeled in type 2 inflammation (**Figure 2A, B and S2A**), highlighting both known and unique responses. Mast cell expansion, a well-established feature of allergic reactions (Brandt et al., 2003), was observed in OVA-treated mice (adjusted $P = 1.03*10^{-11}$,

Wald test, **Figure 2B**) and validated by flow cytometry (**Figure 2C**, $P = 0.005$, *t*-test). We also observed a significant increase in ILC2 frequency in mice with type 2 immune reactions to OVA (**Figure 2B**, $P = 1.22*10^{-2}$, Wald test), which we validated by flow cytometry (**Figure 2D**, $P = 0.009$, *t*-test), highlighting their importance in this allergic inflammatory model (Burton et al., 2018). Macrophage and neutrophil frequencies also increased significantly in OVA-treated mice ($P = 3.87*10^{-3}$ and $P = 4.15*10^{-3}$, respectively, Wald test), reflecting immune cell infiltration. $CD11b^{+}CD103^{+}$ DCs, one of four different populations of DCs in the intestine (Mowat and Agace, 2014), were the most significantly reduced by OVA-induced inflammation ($P = 6.04*10^{-8}$, Wald test), suggesting that they were likely involved in the maintenance of gut homeostasis, and suppressed in the type 2 inflammatory condition.

The impact of type 2 inflammation on cell intrinsic expression changes was primarily centered in mast cells and ILC2s in both LP and PP regions (**Figure 2E** and **Table S3**). Genes associated with cell type-specific activation were induced in mast cells (*e.g., Mcpt1*, *Mcpt4*) and ILC2s (*e.g., Il13, Il4*) (**Figure S2B**), suggesting an activation phenotype in both cell types. In addition, *Ighg1* and *Ighe* expression in plasma cells was significantly increased ($P=1.45*10^{-107}$ and $2.86*10^{-13}$, respectively; likelihood ratio test) after the induction of allergic inflammation (**Figure S2C**), consistent with the fact that IL-4 induces class-switch recombination of immunoglobulin heavy (Ig) chain towards IgG1 and IgE (Manis et al., 2002). Additionally, genes involved in the type 1 interferon pathway, such as *Irf1* and *Isg15* in macrophages and *Ifnar1* and *Ifitm3* in plasma cells, were suppressed during type 2 inflammation (**Figure S2B**), providing potential mechanistic explanations for the dampened antiviral immunity in allergic inflammation (Kloepfer et al., 2012; Rowe and Gill, 2015).

Topic models identify cell type-specific programs that are increased with inflammation in mast cells, ILC2s, Th2 cells and fibroblast subsets

To identify more nuanced changes in expression programs in response to type 2 inflammation, we relied on topic modeling using Latent Dirichlet Allocations (Blei et al., 2003), which has recently been applied to scRNA-seq data (Bielecki et al., 2018; duVerle et al., 2016). Originally developed to discover key semantic topics reflected by the words used in a corpus of documents (Dumais et al., 1990), topic modeling can be used to explore gene programs ("topics") in each cell ("document") based on the distribution of genes ("words") expressed in the cell. A gene can belong to multiple programs, and its relative relevance in the topic is reflected by a weight. A cell is then represented as a weighted mixture of topics, where the weights reflect the importance of the corresponding gene program in the cell. We learned topic models for each cell lineage or group separately, and then searched for topics that were differentially weighted between homeostasis and inflammation in cells of the same type (**STAR Methods**, **Table S4, Figure 3A-E and S3A-F**).

Topics specifically characterizing activation in mast cells and ILC2s increased in prominence following inflammation. Topic 1 ("mast cell activation program"), which was heavily weighted in the mast cell cluster among myeloid cells, was characterized by *Cpa3* and *Mcpt4* expression and significantly more prominent in mast cells from mice treated with OVA than controls (adjusted $P = 2.84*10^{-67}$, Mann–Whitney U test, **Figure 3A**). Topic 2 ("ILC2 activation program"), which was heavily weighted in the ILC2 cluster, included type 2 genes such as *Il13* and *Il4*. Topic 2 was significantly more prominent in ILC2s after induction of inflammation (adjusted $P = 8.01*10^{-12}$, Mann–Whitney U test, **Figure 3B**). Consistent with our differential expression analysis, these two topics captured the major events induced by inflammation.

Programs related to inflammatory responses were also more heavily weighted in Th2 cells under inflammatory conditions, whereas those related to T regulatory cells were unchanged between inflammation and homeostasis. Specifically, topic 5 ("Th2 inflammatory program"),

consisting of type 2 inflammatory genes, including *Il13, Gata3, Il6, Areg* and *Il1rl1*, was present only in a subset of cells from the activated $CD4^+$ T cell cluster that were likely type 2 T helper (T_H2) cells (**Figure 3C**). Topic 5 weights were significantly higher in cells from OVA-treated mice than from controls (adjusted $P = 2.73*10^{-5}$, Mann–Whitney U test, **Figure 3C**). Topic 9 ("T regulatory program"), comprised of *Foxp3, Lag3, Il10* and other Th regulatory genes, was present in a different subset of $CD4^+$ T cells (**Figure 3D**), but its weight showed only a minor change with inflammation (adjusted $P = 0.002$, Mann–Whitney U test, **Figure 3D**). This suggests that activation of type 2 inflammation in this model did not significantly interfere with the activity of regulatory T cells.

Topic 4 from stromal cells, defined by the expression of the type 2 inflammatory cytokine *Il33* and key chemokines such as *Ccl21a*, was uniquely associated with fibroblasts and increased in weight with inflammation (**Figure 3E**, adjusted $P = 2.69*10^{-5}$, Mann–Whitney U test). We confirmed that IL-33 and CCL21 were co-expressed in $PDPN^+$ stromal cells by immunofluorescence (**Figure S3G**). Moreover, the number of $IL\text{-}33^+PDPN^+$ intestinal fibroblasts was significantly increased in mice under type 2 inflammation induced by OVA (**Figure 3F**, $P = 0.002$, *t*-test), indicating that stromal cell-derived IL-33 may play critical roles in promoting intestinal type 2 inflammation.

Calca-encoded α-CGRP expression is a key feature of the ILC2 activation program induced by inflammation, but its receptor is repressed by inflammation

Calca was the highest and most uniquely scoring gene in the ILC2 activation program (**Figure 3B**) and *Calca* transcript levels were highest in ILC2s among all cell types in our dataset (**Figure 4A** and **S4A**). Exons 4 and 5 of *Calca* encode the neuropeptides calcitonin (CT) and α-CGRP, respectively, via alternative splicing (Amara et al., 1982). Quantitative PCR (qPCR)

revealed that while CT-encoding exon 4 was expressed in intestinal KLRG1$^+$ ILC2s at steady state (**Figure S4B**), α-CGRP-encoding exon 5 was detectable only following induction of a type 2 inflammatory reaction to OVA (P = 0.01, t-test) (**Figure 4B**). Conversely, the corresponding transcripts of α-CGRP receptor components — a G-protein-coupled receptor complex consisting of CRLR and RAMP1 — were expressed in ILC2s at steady state (**Figure 4B** and **S4A**), but significantly repressed by type 2 inflammation (**Figure 4B**, P = 0.005 and 0.02 for *Calcrl* and *Ramp1*, respectively, t test). The *Calcr* transcript, encoding the CT receptor, was not detectable by either scRNA-seq or qPCR (data not shown). Taken together, these results are consistent with a negative feedback model, where signaling through α-CGRP to ILC2s suppresses its receptor's expression in the cells, and suggest that an α-CGRP-mediated signaling pathway may regulate ILC2 activity in type 2 immune responses.

α-CGRP suppresses type 2 inflammation-induced activation and expansion of ILC2s *in vitro* and *in vivo*

To determine if α-CGRP can directly trigger signaling in ILC2s and impact their transcriptional states under inflammatory conditions, we performed bulk RNA-seq of KLRG1$^+$ ILC2s isolated from the small intestine and stimulated *in vitro* with IL-25 alone or together with α-CGRP. As expected, IL-25 alone induced the expected activation phenotype, including expression of type 2 cytokines, such as *Il13* and *Il5*, and key mitotic genes, such as *Myc* (**Figure 4C**). Strikingly, this IL-25-induced activation signature was significantly suppressed when cells were treated with both IL-25 and α-CGRP (**Figure 4C,D**, adjusted P < 0.001, t-test), with the exception of a few genes, notably *Il5*, which was further induced (**Figure 4C** and **S4C**). Moreover, α-CGRP co-treatment significantly suppressed IL-25-induced cell division (**Figure 4E**, P = 0.01, t-test). Thus, α-CGRP inhibits IL-25-induced proliferation and activation of intestinal KLRG1$^+$ ILC2s.

We next used an IL-25-induced *in vivo* activation model (Huang et al., 2015) (**Figure 5A**) to show that α-CGRP suppresses expansion of ILC2s responding to inflammation. Intraperitoneal administration of α-CGRP impaired IL-25-induced expansion of KLRG1$^+$ ILC2s (**Figure 5B** and **S5A**), consistent with our *in vitro* results. Recent work has shown that intestinal KLRG1$^+$ ILC2s can migrate to mesenteric lymph nodes (mLNs) and other tissues during inflammation via sphingosine 1-phosphate (S1P)-mediated chemotaxis (Huang et al., 2018). To determine whether α-CGRP primarily impacts intestinal or mLN ILC2s, we relied on the fact that intestinal GATA3$^+$ ILC2s are generally phenotypically KLRG1$^+$ST2$^-$ (data not shown), whereas mLN ILC2s are mainly ST2$^+$ at steady state (**Figure 5C**). IL-25 administration increased the frequency of both KLRG1$^+$ST2$^-$ inflammatory ILC2s and ST2$^+$ ILC2s in mLNs (**Figure 5C-E** and **S5B**). But co-administration with α-CGRP only reduced the frequency of KLRG1$^+$ST2$^-$ ILC2s (**Figure 5C,D** and **S5B**), which are cells that migrated from the small intestine to the mLNs, but not of ST2$^+$ ILC2s (**Figure 5E**). Thus, α-CGRP preferentially regulates the response of intestinal KLRG1$^+$ST2$^-$ ILC2s. Furthermore, α-CGRP also significantly suppressed the expansion of intestinal ILC2s in a food allergy model (**Figure 5F,G** and **S5C**,**D**, P = 0.02 for **5G**, P = 0.009 for **S5D**, *t*-test), where we intragastrically administrated α-CGRP together with OVA into pre-sensitized mice. Taken together, α-CGRP antagonized expansion of intestinal KLRG1$^+$ ILC2s in two different type 2 inflammatory models.

At homeostasis, α-CGRP is predominantly expressed *in vivo* in two subsets of Chat$^+$ enteric neurons

Without inflammation, intestinal KLRG1$^+$ ILC2s expressed CGRP receptors (**Figure 4B**), but not CGRP, leading us to search for neighboring cell type(s) which potentially produce CGRP at homeostasis. To this end, we analyzed *Calca* gene expression across multiple intestinal

scRNA-seq datasets, including our previous epithelial atlas for the mouse small intestine epithelium (Haber et al., 2017) (**Figure S6A**), our intestinal immune atlas here (**Figure 1**), and scRNA-Seq of enteric neurons from *Wnt1-Cre:R26Tomato* mice (Zeisel et al., 2018) (**Figure 6A** and **S6B,C**). *Calca* expression was only detected in two subsets of $ChAT^+$ enteric neurons (**Figure 6B** and **S6C**). These $ChAT^+$ enteric neurons also expressed (**Figure 6B**): (**1**) the CGRP receptor genes, (**2**) the *Calcb* gene, encoding β-CGRP peptide, which differs in two amino acid from α-CGRP, but has not been substantially studied for its function in immune cells, and (**3**) the *Nmu* gene, which we and others have shown amplifies the activity of ILC2s under type 2 inflammation in the lung and small intestine (Cardoso et al., 2017; Klose et al., 2017; Wallrapp et al., 2017).

We confirmed by immunofluorescence staining that $ChAT^+$ enteric neurons expressed CGRP (**Figure 6C**), and that ILC2s contact with CGRP-expressing neurons at the steady state (**Figure S6D**), consistent with previous reports that ILC2s are closely associated with neurons in the intestine (Klose et al., 2017). Thus, CGRP from these $ChAT^+$ enteric neurons may regulate ILC2 homeostasis.

α-CGRP suppresses ILC2 proliferation through activating a cAMP response module

The presence at homeostasis of α-CGRP receptors on ILC2s and α-CGRP's expression on $ChAT^+$ intestinal neurons led us to hypothesize that it has an effect on ILC2s during homeostasis. To test this hypothesis, we next measured the expression profiles of intestinal $KLRG1^+$ ILC2s stimulated *in vitro* by α-CGRP alone, and identified genes differentially expressed under this signal (**Figure 6D**, **Methods**).

Analyzing the profiles suggested that α-CGRP activated a cAMP response module. First, α-CGRP stimulation induced expression of key genes involved in adenylate cyclase-mediated GPCR signaling, including *Adrb2, Adora2a, Pde4b* and *Akap12* (**Figure 6D**), as well as cAMP response genes, including *Areg* (Shao and Sheng, 2010), *Crem*, and *Il5* (**Figure 6D**). Indeed, previous studies showed that cAMP directly induces IL5 expression in ILC2s (Nussbaum et al., 2013). Consistently, ATAC-Seq profiling of ILC2s revealed that regions of increased chromatin accessibility following α-CGRP stimulation alone where enriched for gene loci involved in the adenylate cyclase pathway (**Figure 6E and Table S5**).

Moreover, α-CGRP stimulation *in vitro* negatively regulated ILC2 proliferation, and this effect may be mediated by induction of genes involved in cell cycle arrest in the cAMP response module. In our KLRG1^{+} ILC2 cells, α-CGRP induced expression of genes involved in cell cycle arrest, such as *Cdkn1a*, *Gadd45a* and *Akap12*, as well as of key negative regulators of ILC2 expansion, *Adrb2* and *Pdcd1* (Moriyama et al., 2018; Taylor et al., 2017) (**Figure 6D**). cAMP and its principal target, cAMP-dependent protein kinase (PKA), have been previously shown to suppress proliferation via negatively regulating mitogen-activated protein (MAP) kinase cascade in a cell context-dependent manner (Stork and Schmitt, 2002). Indeed, the adenylate cyclase activator forskolin, which increases intracellular cAMP levels (Rodriguez et al., 2013), suppressed the proliferation of ILC2s (**Figure 6F**), but not their viability (**Figure 6G).** Furthermore, treating ILC2s with an adenylate cyclase inhibitor (Klein et al., 2012) partially rescued the cell proliferation defect mediated by α-CGRP (**Figure 6H**). Taken together, our data suggest that α-CGRP suppresses ILC2 proliferation via activating a cAMP response module.

At homeostasis, α-CGRP maintains ILC2 and type 2 responses *in vivo*

Finally, we tested if α-CGRP-mediated signaling regulates homeostasis of intestinal KLRG1$^+$ ILC2s at steady state *in vivo*, by analyzing α-CGRP exon knockout (α-CGRP KO) mice, in which the CT exon of *Calca* gene remains intact (Oh-hashi et al., 2001). The frequency of intestinal KLRG1$^+$ ILC2s was significantly increased in α-CGRP KO mice compared to wild type (WT) controls (P = 0.002, *t*-test) (**Figure 6I**). Type-2 cytokines promote differentiation of tuft cells (Biton et al., 2018; Gerbe et al., 2016; Howitt et al., 2016; von Moltke et al., 2016), and the number of tuft cells was indeed also significantly increased in α-CGRP KO mice (P = 0.036, *t*-test) (**Figure 6J**). Thus, α-CGRP-mediated signaling helped maintain the homeostasis of KLRG1$^+$ ILC2s and type 2 immunity in the small intestine.

DISCUSSION

Here, we collected and analyzed a scRNA-seq atlas of immune cells in the small intestine in homeostasis and during type 2 inflammation, uncovered dynamic responses in cell type-specific programs that monitor and titrate mucosal responses, and identified α-CGRP as a key regulator impacting the frequency and activity of intestinal KLRG1$^+$ ILC2s.

Our work highlights a role for α-CGRP in regulating ILC2s at both homeostasis and during inflammation. Previous studies showed that CGRP signaling can generate both pro- and anti-inflammatory immune responses, depending on cell type, tissue and experimental model (Assas et al., 2014). α-CGRP increases IL-5 expression in lung ILC2s co-stimulated with IL-33 (Sui et al., 2018). Mice with deficiency in CRLR in IL-5-expressing cells manifest a normal frequency of ST2$^+$ ILC2s in lungs exposed to house dust mite (HDM) (Sui et al., 2018), consistent with our finding that ST2$^+$ ILC2s in mLNs are not significantly affected by α-CGRP administration. However, our work further reveals that α-CGRP reduced the expansion of intestinal ST2$^-$KLRG1$^+$ ILC2s in two different inflammatory models. Although differences in

cell states between lung $ST2^+$ and intestinal $ST2^-$ $KLRG1^+$ ILC2s (Ricardo-Gonzalez et al., 2018) might contribute to their differential reactions to CGRP signaling, additional studies in animal models where CRLR is specifically-deleted in intestinal $KLRG1^+$ ILC2s will be needed to elucidate the full molecular mechanism. In addition, it will be important to compare the effects of α-CGRP *vs*. β-CGRP binding to CRLR in ILC2s.

We show that two subsets of $ChAT^+$ enteric neurons are the predominant source of CGRP in the small intestine at steady state. In addition to multiple neuropeptides, these $ChAT^+$ neurons also express *Il13ra1* and *Il4ra* (**Figure S6C**), which encode the components of the receptor complex for the type 2 cytokine IL-13. Thus, these $ChAT^+$ neurons may be specialized for crosstalk with the immune system. Future studies will help determine if cytokine signaling from immune cells during inflammation further boosts the secretion of neuropeptides.

CGRP signaling is an additional key axis of neuro-immune interaction with implications for inflammation, including food allergy. Neuronal signals are emerging as important orchestrators of immune responses in the gastrointestinal tract (Chesne et al., 2018; Godinho-Silva et al., 2018; Veiga-Fernandes and Mucida, 2016). In particular, the nervous system has been shown to exercise dual functions to either activate or inhibit ILC2s via different GPCRs. While NMUR1 signaling amplifies ILC2 activation in the lung and intestines (Cardoso et al., 2017; Klose et al., 2017; Wallrapp et al., 2017), the β2-adrenergic receptor (β_2AR) pathway negatively regulates ILC2 expansion (Moriyama et al., 2018).

We thus propose a model for how ILC2s integrate and balance such diverse neural signaling cues, involving different Gα proteins and their downstream signaling (**Figure 7**). In this model, the amplifier NMUR1 mainly signals through $G\alpha_{q/11}$ and inhibits cAMP levels (Martinez and O'Driscoll, 2015), whereas the negative regulators CRLR and β_2AR are both coupled with $G\alpha_s$

proteins that activate adenylate cyclase and the cAMP pathway (Chatterjee et al., 1993; Madamanchi, 2007). Intracellular cAMP accumulation induces expression of the cAMP response module including IL-5, but suppresses ILC2 proliferation. Thus, selective activation of different subgroups of α subunits of G proteins coupled with variable downstream effects, including the concentration of cAMP, might be utilized by ILC2s to fine-tune the response to neuronal signaling.

Collectively, our work underscores the importance of α-CGRP suppression of ILC2 activity, which may serve as a therapeutic target for treating diseases like food allergy. Since monoclonal antibodies against CGRP have been recently approved to treat migraine (Edvinsson, 2018), it will be important to monitor for the incidence of allergic diseases in treated patients. More broadly, our work provides a resource for understanding the intestinal immune system in response to type 2 inflammation in the context of each specific cell type. Further exploration of the atlas can lead to additional hypotheses on circuits within and between additional cell types that contribute to type 2 immune responses.

ACKNOWLEDGMENTS

We thank Leslie Gaffney and Anna Hupalowska for help with figures, Tim Tickle for help with the Single Cell Portal, Dr. Hans Oettgen (Boston Children's Hospital) for discussions, and the Broad Flow Cytometry Facility (Patricia Rogers, Stephanie Saldi and Chelsea Otis). Work was supported by the Food Allergy Science Initiative (A.R. and R.J.X.), the Klarman Cell Observatory (AR) and HHMI (AR).

AUTHOR CONTRIBUTIONS

H.X., R.J.X. and A.R. conceived the study. A.R. and R.J.X. supervised this study. H.X. designed and performed all experiments. J.D. performed computational analysis with contributions from C.P., H.X., O.A., and M.T., and guidance from A.R. A.W., C.S., P.R.B., H.N.S. and V.K.K. helped with animal works. S.M. assisted with ATAC-seq. D.D., L.T.N., and O.R.-R. assisted with scRNA-seq. A.L. assisted with bulk RNA-seq. H.X., A.R., and R.J.X. wrote the manuscript with input from all authors.

DECLARATION OF INTERESTS

A.R. is a SAB member of ThermoFisher Scientific and Syros Pharmaceuticals. A.R. and R.J.X. are cofounders of and equity holders in Celsius Therapeutics. H.X., R.J.X. and A.R. are co-inventors on US provisional patent application no. 62/667,381 filed by The Broad Institute relating to the subject matter of this manuscript.

REFERNCES

Amara, S.G., Jonas, V., Rosenfeld, M.G., Ong, E.S., and Evans, R.M. (1982). Alternative RNA processing in calcitonin gene expression generates mRNAs encoding different polypeptide products. Nature *298*, 240-244.

Artis, D., and Spits, H. (2015). The biology of innate lymphoid cells. Nature *517*, 293-301.

Assas, B.M., Pennock, J.I., and Miyan, J.A. (2014). Calcitonin gene-related peptide is a key neurotransmitter in the neuro-immune axis. Front Neurosci *8*, 23.

Bielecki, P., Riesenfeld, S.J., Kowalczyk, M.S., Amezcua Vesely, M.C., Kroehling, L., Yaghoubi, P., Dionne, D., Jarret, A., Steach, H.R., McGee, H.M., *et al.* (2018). Skin inflammation driven by differentiation of quiescent tissue-resident ILCs into a spectrum of pathogenic effectors. bioRxiv.

Biton, M., Haber, A.L., Rogel, N., Burgin, G., Beyaz, S., Schnell, A., Ashenberg, O., Su, C.W., Smillie, C., Shekhar, K., *et al.* (2018). T Helper Cell Cytokines Modulate Intestinal Stem Cell Renewal and Differentiation. Cell *175*, 1307-1320 e1322.

Blei, D.M., Ng, A.Y., and Jordan, M.I. (2003). Latent Dirichlet allocation. J Mach Learn Res *3*, 993-1022.

Brandt, E.B., Strait, R.T., Hershko, D., Wang, Q., Muntel, E.E., Scribner, T.A., Zimmermann, N., Finkelman, F.D., and Rothenberg, M.E. (2003). Mast cells are required for experimental oral allergen-induced diarrhea. The Journal of clinical investigation *112*, 1666-1677.

Burton, O.T., Medina Tamayo, J., Stranks, A.J., Miller, S., Koleoglou, K.J., Weinberg, E.O., and Oettgen, H.C. (2018). IgE promotes type 2 innate lymphoid cells in murine food allergy. Clin Exp Allergy *48*, 288-296.

Cardoso, V., Chesne, J., Ribeiro, H., Garcia-Cassani, B., Carvalho, T., Bouchery, T., Shah, K., Barbosa-Morais, N.L., Harris, N., and Veiga-Fernandes, H. (2017). Neuronal regulation of type 2 innate lymphoid cells via neuromedin U. Nature *549*, 277-281.

Chatterjee, T.K., Moy, J.A., Cai, J.J., Lee, H.C., and Fisher, R.A. (1993). Solubilization and characterization of a guanine nucleotide-sensitive form of the calcitonin gene-related peptide receptor. Mol Pharmacol *43*, 167-175.

Chesne, J., Cardoso, V., and Veiga-Fernandes, H. (2018). Neuro-immune regulation of mucosal physiology. Mucosal Immunol.

Ding, J., Condon, A., and Shah, S.P. (2018). Interpretable dimensionality reduction of single cell transcriptome data with deep generative models. Nature communications *9*, 2002.

Dumais, S.T., Furnas, G.W., Landauer, T.K., and Harshman, R. (1990). Indexing by Latent Semantic Analysis. Journal of the American Society for Information Science *41*, 391-407.

duVerle, D.A., Yotsukura, S., Nomura, S., Aburatani, H., and Tsuda, K. (2016). CellTree: an R/bioconductor package to infer the hierarchical structure of cell populations from single-cell RNA-seq data. BMC Bioinformatics *17*, 363.

Edvinsson, L. (2018). CGRP Antibodies as Prophylaxis in Migraine. Cell *175*, 1719.

Gerbe, F., Sidot, E., Smyth, D.J., Ohmoto, M., Matsumoto, I., Dardalhon, V., Cesses, P., Garnier, L., Pouzolles, M., Brulin, B., *et al.* (2016). Intestinal epithelial tuft cells initiate type 2 mucosal immunity to helminth parasites. Nature *529*, 226-230.

Gieseck, R.L., 3rd, Wilson, M.S., and Wynn, T.A. (2018). Type 2 immunity in tissue repair and fibrosis. Nature reviews Immunology *18*, 62-76.

Godinho-Silva, C., Cardoso, F., and Veiga-Fernandes, H. (2018). Neuro-Immune Cell Units: A New Paradigm in Physiology. Annual review of immunology.

Haber, A.L., Biton, M., Rogel, N., Herbst, R.H., Shekhar, K., Smillie, C., Burgin, G., Delorey, T.M., Howitt, M.R., Katz, Y., *et al.* (2017). A single-cell survey of the small intestinal epithelium. Nature *551*, 333-339.

Hammad, H., and Lambrecht, B.N. (2015). Barrier Epithelial Cells and the Control of Type 2 Immunity. Immunity *43*, 29-40.

Hepworth, M.R., Monticelli, L.A., Fung, T.C., Ziegler, C.G., Grunberg, S., Sinha, R., Mantegazza, A.R., Ma, H.L., Crawford, A., Angelosanto, J.M., *et al.* (2013). Innate lymphoid cells regulate CD4+ T-cell responses to intestinal commensal bacteria. Nature *498*, 113-117.

Howitt, M.R., Lavoie, S., Michaud, M., Blum, A.M., Tran, S.V., Weinstock, J.V., Gallini, C.A., Redding, K., Margolskee, R.F., Osborne, L.C., *et al.* (2016). Tuft cells, taste-chemosensory cells, orchestrate parasite type 2 immunity in the gut. Science *351*, 1329-1333.

Huang, Y., Guo, L., Qiu, J., Chen, X., Hu-Li, J., Siebenlist, U., Williamson, P.R., Urban, J.F., Jr., and Paul, W.E. (2015). IL-25-responsive, lineage-negative KLRG1(hi) cells are multipotential 'inflammatory' type 2 innate lymphoid cells. Nature immunology *16*, 161-169.

Huang, Y., Mao, K., Chen, X., Sun, M.A., Kawabe, T., Li, W., Usher, N., Zhu, J., Urban, J.F., Jr., Paul, W.E., *et al.* (2018). S1P-dependent interorgan trafficking of group 2 innate lymphoid cells supports host defense. Science *359*, 114-119.

Klein, M., Vaeth, M., Scheel, T., Grabbe, S., Baumgrass, R., Berberich-Siebelt, F., Bopp, T., Schmitt, E., and Becker, C. (2012). Repression of cyclic adenosine monophosphate upregulation disarms and expands human regulatory T cells. Journal of immunology *188*, 1091-1097.

Kloepfer, K.M., Olenec, J.P., Lee, W.M., Liu, G., Vrtis, R.F., Roberg, K.A., Evans, M.D., Gangnon, R.E., Lemanske, R.F., Jr., and Gern, J.E. (2012). Increased H1N1 infection rate in children with asthma. Am J Respir Crit Care Med *185*, 1275-1279.

Klose, C.S.N., Mahlakoiv, T., Moeller, J.B., Rankin, L.C., Flamar, A.L., Kabata, H., Monticelli, L.A., Moriyama, S., Putzel, G.G., Rakhilin, N., *et al.* (2017). The neuropeptide neuromedin U stimulates innate lymphoid cells and type 2 inflammation. Nature *549*, 282-286.

Kotas, M.E., and Locksley, R.M. (2018). Why Innate Lymphoid Cells? Immunity *48*, 1081-1090.

Locksley, R.M. (2010). Asthma and allergic inflammation. Cell *140*, 777-783.

Madamanchi, A. (2007). Beta-adrenergic receptor signaling in cardiac function and heart failure. Mcgill J Med *10*, 99-104.

Manis, J.P., Tian, M., and Alt, F.W. (2002). Mechanism and control of class-switch recombination. Trends in immunology *23*, 31-39.

Martinez, V.G., and O'Driscoll, L. (2015). Neuromedin U: a multifunctional neuropeptide with pleiotropic roles. Clin Chem *61*, 471-482.

Molofsky, A.B., Savage, A.K., and Locksley, R.M. (2015). Interleukin-33 in Tissue Homeostasis, Injury, and Inflammation. Immunity *42*, 1005-1019.

Moriyama, S., Brestoff, J.R., Flamar, A.L., Moeller, J.B., Klose, C.S.N., Rankin, L.C., Yudanin, N.A., Monticelli, L.A., Putzel, G.G., Rodewald, H.R., *et al.* (2018). beta2-adrenergic receptor-mediated negative regulation of group 2 innate lymphoid cell responses. Science *359*, 1056-1061.

Mowat, A.M., and Agace, W.W. (2014). Regional specialization within the intestinal immune system. Nature reviews Immunology *14*, 667-685.

Neill, D.R., Wong, S.H., Bellosi, A., Flynn, R.J., Daly, M., Langford, T.K., Bucks, C., Kane, C.M., Fallon, P.G., Pannell, R., *et al.* (2010). Nuocytes represent a new innate effector leukocyte that mediates type-2 immunity. Nature *464*, 1367-1370.

Nussbaum, J.C., Van Dyken, S.J., von Moltke, J., Cheng, L.E., Mohapatra, A., Molofsky, A.B., Thornton, E.E., Krummel, M.F., Chawla, A., Liang, H.E., *et al.* (2013). Type 2 innate lymphoid cells control eosinophil homeostasis. Nature *502*, 245-248.

Oh-hashi, Y., Shindo, T., Kurihara, Y., Imai, T., Wang, Y., Morita, H., Imai, Y., Kayaba, Y., Nishimatsu, H., Suematsu, Y., *et al.* (2001). Elevated sympathetic nervous activity in mice deficient in alphaCGRP. Circ Res *89*, 983-990.

Price, A.E., Liang, H.E., Sullivan, B.M., Reinhardt, R.L., Eisley, C.J., Erle, D.J., and Locksley, R.M. (2010). Systemically dispersed innate IL-13-expressing cells in type 2 immunity. Proceedings of the National Academy of Sciences of the United States of America *107*, 11489-11494.

Pulendran, B., and Artis, D. (2012). New paradigms in type 2 immunity. Science *337*, 431-435.
Ricardo-Gonzalez, R.R., Van Dyken, S.J., Schneider, C., Lee, J., Nussbaum, J.C., Liang, H.E., Vaka, D., Eckalbar, W.L., Molofsky, A.B., Erle, D.J., *et al.* (2018). Tissue signals imprint ILC2 identity with anticipatory function. Nature immunology *19*, 1093-1099.

Robinette, M.L., Fuchs, A., Cortez, V.S., Lee, J.S., Wang, Y., Durum, S.K., Gilfillan, S., Colonna, M., and Immunological Genome, C. (2015). Transcriptional programs define molecular characteristics of innate lymphoid cell classes and subsets. Nature immunology *16*, 306-317.

Rodriguez, G., Ross, J.A., Nagy, Z.S., and Kirken, R.A. (2013). Forskolin-inducible cAMP pathway negatively regulates T-cell proliferation by uncoupling the interleukin-2 receptor complex. The Journal of biological chemistry *288*, 7137-7146.

Rowe, R.K., and Gill, M.A. (2015). Asthma: the interplay between viral infections and allergic diseases. Immunol Allergy Clin North Am *35*, 115-127.

Rydyznski, C.E., Cranert, S.A., Zhou, J.Q., Xu, H., Kleinstein, S.H., Singh, H., and Waggoner, S.N. (2018). Affinity Maturation Is Impaired by Natural Killer Cell Suppression of Germinal Centers. Cell reports *24*, 3367-3373 e3364.

Shao, J., and Sheng, H. (2010). Amphiregulin promotes intestinal epithelial regeneration: roles of intestinal subepithelial myofibroblasts. Endocrinology *151*, 3728-3737.

Spencer, S.P., Wilhelm, C., Yang, Q., Hall, J.A., Bouladoux, N., Boyd, A., Nutman, T.B., Urban, J.F., Jr., Wang, J., Ramalingam, T.R., *et al.* (2014). Adaptation of innate lymphoid cells to a micronutrient deficiency promotes type 2 barrier immunity. Science *343*, 432-437.

Stork, P.J., and Schmitt, J.M. (2002). Crosstalk between cAMP and MAP kinase signaling in the regulation of cell proliferation. Trends Cell Biol *12*, 258-266.

Sui, P., Wiesner, D.L., Xu, J., Zhang, Y., Lee, J., Van Dyken, S., Lashua, A., Yu, C., Klein, B.S., Locksley, R.M., *et al.* (2018). Pulmonary neuroendocrine cells amplify allergic asthma responses. Science.

Tanay, A., and Regev, A. (2017). Scaling single-cell genomics from phenomenology to mechanism. Nature *541*, 331-338.

Taylor, S., Huang, Y., Mallett, G., Stathopoulou, C., Felizardo, T.C., Sun, M.A., Martin, E.L., Zhu, N., Woodward, E.L., Elias, M.S., *et al.* (2017). PD-1 regulates KLRG1+ group 2 innate lymphoid cells. The Journal of experimental medicine *214*, 1663-1678.

Tordesillas, L., Berin, M.C., and Sampson, H.A. (2017). Immunology of Food Allergy. Immunity *47*, 32-50.

Veiga-Fernandes, H., and Mucida, D. (2016). Neuro-Immune Interactions at Barrier Surfaces. Cell *165*, 801-811.

von Moltke, J., Ji, M., Liang, H.E., and Locksley, R.M. (2016). Tuft-cell-derived IL-25 regulates an intestinal ILC2-epithelial response circuit. Nature *529*, 221-225.

Wagner, A., Regev, A., and Yosef, N. (2016). Revealing the vectors of cellular identity with single-cell genomics. Nat Biotechnol *34*, 1145-1160.

Wallrapp, A., Riesenfeld, S.J., Burkett, P.R., Abdulnour, R.E., Nyman, J., Dionne, D., Hofree, M., Cuoco, M.S., Rodman, C., Farouq, D., *et al.* (2017). The neuropeptide NMU amplifies ILC2-driven allergic lung inflammation. Nature *549*, 351-356.

Zeisel, A., Hochgerner, H., Lonnerberg, P., Johnsson, A., Memic, F., van der Zwan, J., Haring, M., Braun, E., Borm, L.E., La Manno, G., *et al.* (2018). Molecular Architecture of the Mouse Nervous System. Cell *174*, 999-1014 e1022.

Figure legends

Figure 1. A single-cell expression atlas of intestinal immune cells

(A) Overview. The lamina propria (LP) and Peyer's patch (PP) regions of the small intestine were harvested from mice in homeostasis ("healthy") or after induction of a type 2 inflammatory reaction to ovalbumin (OVA) ("inflamed") (left). After enzymatic tissue dissociation, immune cells were captured by fluorescence-activated cell sorting (FACS) (middle) and analyzed by droplet-based 3′scRNA-seq (right).

(B) Cell subsets in the intestinal immune cell atlas. scvis learned two-dimensional (2D) representation of 58,067 cell profiles (dots) from both PP and LP regions, colored and numbered by cluster membership. Clustered are rank ordered by size (from the largest of 7194, cluster 1, to the smallest of 17, cluster 46). DZ, dark zone; LZ, light zone; DN, double negative; C1, cluster 1; C2, cluster 2.

(C) Differentially expressed genes. For representative differentially expressed genes (rows) across clusters (columns), shown is the fraction of cells in the cluster that express a gene (dot size) and the z-score of the mean expression of that gene in the cluster (color; z-score of average $\log_2(\text{TPM}+1)$).

(D) Tissue distribution of non-T and non-B immune cells in homeostasis. Proportion (*y* axis) of each cell type in LP (red) and PP (black) regions. Points: independent experiments; Box-and-whisker plots show the median, quartiles, and range. *$p < 4.8\times10^{-3}$, **$p < 3.8\times10^{-6}$, ***p

$< 4.3\times10^{-7}$, Wald test.

(E) LTi cells are enriched in PP regions. Shown is flow cytometry analysis gated on $CD45^{+}Lin^{-}$ $CD90.2^{+}IL7R^{+}ROR\gamma t^{+}$ cells. Left: Numbers adjacent to outlined areas indicate percent ILC3 (left) or LTi cells (right). Right: Summary of results. n = 3 mice, mean and SEM; ***p < 0.001, Fisher's exact test.

Figure 2. Increased ILC2 proportions and changes in ILC2 programs are key features in OVA-induced type 2 inflammation

(A-D) Increased ILC2 and mast cell frequencies are prominent features in type 2 inflammation. (A) A 2D embedding as in **Figure 1B**, where each cell profile (dot) is colored by whether it was obtained in homeostatic (black) or OVA-induced inflammatory (red) conditions. (B) Distribution of cell type proportions (y axis) for each non-T and non-B cell subset (x axis) in homeostatic (black) or inflammatory (red) conditions. Points: independent experiments. Box-and-whisker plots show the median, quartiles, and range. *p < 1.3×10^{-2}, **p < 4.5×10^{-4}, ***p < 6.1×10^{-8}, Wald test. (C and D) Flow cytometry analysis of frequencies of mast cells (C, gated on $CD45^{+}Lin^{-}$) and ILC2s (D, gated on $CD45^{+}Lin^{-}CD90.2^{+}IL7R^{+}$) in mice treated with PBS (black) or OVA (red). Left: representative FACS plots; Right: summary of results. Points: individual mice; data are from two independent experiments. mean and SEM; **p < 0.01, Student's *t* test.

(E) ILC2s and mast cells show the most prominent changes in expression programs in type 2 inflammation. Number of genes significantly induced (black) or inhibited (grey) (|fold change| ≥ 2, FDR < 0.05, expressed at least in 25% of cells at the up-regulation side; color bar) by OVA-induced type 2 inflammation in each cell subset (column) from the LP or PP regions (label on left).

Figure 3. Topic modeling of cell type-specific programs in response to intestinal type 2 inflammation predicts *Calca* as a top gene in ILC2s

(A-E) Inflammation associated programs in specific cell subsets. Shown are some of the topics that have differential scores between steady state (PBS) and inflammatory conditions (OVA) for myeloid cells (A), ILCs (B), T cells (C, D) or stromal cells (E). Left: Bar plot shows the score (x axis) of top ranked genes for this topic (y axis). Top right: a portion of the 2D embedding in **Figure 1B**, showing only cells from the noted subset cells, colored by the topic's weight in the cell (top right). Bottom right: empirical cumulative density function (y axis) of topic weights (x axis) for cells from mice treated with PBS (black curve) or OVA (red curve). p values: Mann–Whitney U test.

(F) Increased number of IL-33^{+}PDPN^{+} fibroblasts in inflammation. Left: Representative IF images of small intestines from mice at steady state (PBS) or inflammatory (OVA) conditions. Arrow, IL-33^{+}PDPN^{+} fibroblasts; Scale bars, 50 μm. Right: Quantified cell densities. Points:

individual mice; data are from two independent experiments. mean and SEM, **p < 0.01, Student's *t* test.

Figure 4. α-CGRP suppresses IL-25-induced activation and expansion of intestinal KLRG1$^+$ ILC2s *in vitro*

(A) Cells expressing *Calca* gene. 2D embedding as in **Figure 1B** where cells (dots) are colored by relative expression of *Calca* ($\log_2$(TPM+1)).

(B) α-CGRP exon specifically induced in inflammation. Expression level (y axis, Quantitative PCR normalized to *Gapdh*) of α-CGRP exon of *Calca* gene, *Calcrl,* and *Ramp1* in intestinal KLRG1$^+$ ILC2s isolated from control (black) or OVA-treated (red) mice. Points: individual experiment; mean and SEM, *p < 0.01, **p < 0.01, Student's *t* test.

(C and D) α-CGRP co-treatment abrogates most of the IL-25 induced response in ILC2s *in vitro.* (C) Expression (color bar, Z score) of genes (rows) significantly induced in ILC2s (Fold change ≥ 2, FDR < 0.05) by IL-25 compared to control, across different conditions (columns).

(D) Box and whisker (min to max) plot of the average Z scores (y axis) of the IL-25-induced genes in (C). ***false discovery rate [FDR] < 0.001, Student's *t* test.

(E) α-CGRP suppresses IL-25-indcued proliferation of ILC2s. Left: Distribution of number of cell divisions (*y* axis, % of maximum observed number) monitored by flow cytometry in KLRG1$^+$ ILC2s labeled with CellTrace Violet and stimulated with IL-25 or IL-25 plus α-CGRP

for 60 hours. Right: Percent of dividing cells (y axis) in each treatment (x axis). Points: individual experiments. mean and SEM, *p < 0.05, Student's *t* test.

Figure 5. α-CGRP antagonizes expansion of intestinal KLRG1$^+$ ILC2s *in vivo*

(A) Experimental design. Mice were intraperitoneally injected with vehicle, lL-25 or IL-25 and α-CGRP daily for two days.

(B) α-CGRP co-treatment antagonizes CD3$^-$KLRG1$^+$ ILC2 expansion *in vivo*. Representative IF images of CD3$^-$KLRG1$^+$ ILC2 (arrows) in small intestines of mice treated as in A. Scale bars, 100 μm. Data are representative of three mice in each condition.

(C-E) α-CGRP antagonizes the expansion of ST2$^-$KLRG1$^+$ ILC2s specifically. (C) Flow cytometry analysis of ILC2s in mLNs cells gated on CD45$^+$Lin$^-$CD90.2$^+$IL7R$^+$ from mice treated as in (A). (D) Frequency (*y* axis) of ST2$^-$KLRG1$^+$ ILC2s in total CD45$^+$ cells in mLNs of mice treated as in A. Points: individual mice. Data from three independent experiments. mean and SEM, *FDR < 0.05, ***FDR < 0.001, Student's *t* test. (E) Frequency (*y* axis) of ST2$^+$ ILC2s in total CD45$^+$ cells in mLNs of mice treated as in A. Point: individual mice. Data are from three independent experiments. mean and SEM, ns: FDR > 0.05, *FDR < 0.05, **FDR < 0.01, Student's *t* test.

(F and G) α-CGRP treatment antagonizes intestinal ILC2 expansion following OVA intraperitoneal sensitization experiment. (F) Experimental overview. (G) Percent of GATA3$^+$

ILC2 (*y* axis) in total $CD45^+$ cells in the small intestine of mice treated as in F. Point: individual mice. Data are from three independent experiments. mean and SEM, *$p < 0.05$, Student's *t* test.

Figure 6. α-CGRP is produced by $ChAT^+$ enteric neurons in steady state and maintains $KLRG1^+$ ILC2 homeostasis *in vivo*

(A and B) $ChAT^+$ enteric neurons express α-CGRP. (A) t-SNE plot of 1105 enteric neuron profiles from *Wnt1-Cre:R26Tomato* mice (Zeisel et al., 2018), where each neuron (dot) is colored by cluster assignment. (B) Distribution of expression levels (y axis, $\log_2$(TPM+1)) of *Nmu*, *Calca*, *Calcb* and *Calcrl* gene in the enteric neurons in each cluster in A (*x* axis).

(C) co-localization of ChAT and CGRP in the small intestines. Representative IF images of the small intestines of wild type mice. Scale bar, 50 μm. Data are representative of three mice.

(D) Expression program induced by α-CGRP in ILC2s *in vitro*. Relative expression (row-wise *Z* score of $\log_2$(FPKM + 1)) of genes (rows) significantly induced or suppressed by α-CGRP stimulation (|Fold change| ≥ 2, FDR < 0.05), across conditions (columns). Key genes are highlighted.

(E) α-CGRP in ILC2s *in vitro* reprograms chromatin accessibility especially at loci of a cAMP response module. Left: Chromatin accessibility ($\log_2$(#cuts+1), **STAR Methods**) of loci (rows) with differential accessibility in ILC2s treated by α-CGRP *vs*. control *in vitro*. Right: Statistical significance (x axis, $-\log_{10}$(q-value)) of molecular functions (y axis) whose associated genes

are enriched in proximity to these differentially accessible ATAC-Seq peaks. Dashed line: q-value = 0.01.

(F and G) Foskolin suppresses ILC2 proliferation but does not impact cell viability. (F) Left: Distribution of number of cell divisions (*y* axis, % of maximum observed number) monitored by flow cytometry in KLRG1$^+$ ILC2s labeled with CellTrace Violet and stimulated with IL-25 and DMSO or forskolin for 40 hours. Right: Percent of divided cells (*y* axis) in each treatment (*x* axis). Points: individual experiments. mean and SEM, ***p < 0.001, Student's *t* test. (G) Left: Cell viability monitored by flow cytometry in cells in F stained with 7AAD. Right: Percent of live (7AAD$^-$) cells (*y* axis) in each treatment (*x* axis). Points: individual experiments. mean and SEM, NS: p > 0.05, Student's *t* test.

(H) Adenylate cyclase inhibitor (SQ22, 536) treatment partially rescues α-CGRP inhibition of ILC2 proliferation. Percent of divided cells (*y* axis) assayed as in F, in ILC2s treated *in vivo* with IL-25 and DMSO alone (black) or with α-CGRP (grey) or α-CGRP+Forskolin (red). Points: individual experiments. mean and SEM, **p < 0.01,*** p< 0.001, Student's *t* test.

(I and J) α-CGRP KO affects ILC2 expansion *in vivo*. (I) Left: Flow cytometry analysis of intestinal KLRG1$^+$ cells among cells gated on CD45$^+$Lin$^-$CD90.2$^+$IL7R$^+$ in α-CGRP WT and KO mice in homeostasis. Right: Percentage of KLRG1$^+$ILC2s (y axis) in α-CGRP WT and KO mice. Points: individual mice. Data from three independent experiments. mean and SEM, **p < 0.01, Student's *t* test. (J) Left: Representative IF images of tuft cells (arrows) in the small

intestine of α-CGRP WT or KO mice. Scale bars, 50 μm. Right: Density of tuft cells (y axis, number per mm^2) in WT and KO. Points: individual mice. Data are from thee independent experiments. mean and SEM, *$p < 0.05$, Student's *t* test.

Figure 7. A model of neuronal signals orchestrating ILC2 responses.

Intestinal ILC2s sense different neuropeptides, including NMU, epinephrine (EPI) and CGRP from enteric neurons via expressing corresponding GPCRs. The amplifier NMUR1 signals through $G\alpha_{q/11}$ and inhibits cAMP level, whereas the negative regulators CRLR and β_2AR are coupled with $G\alpha_s$ protein that results in cAMP accumulation. cAMP suppresses expansion of ILC2s but increases IL-5 expression. Thus, selective activation of different subgroups of α subunits of G proteins coupled with variable concentration of cAMP might be utilized by ILC2s to fine-turn the response to neuronal signaling.

Supplemental Figure legends

Figure S1. FACS, single-cell expression and IF staining analysis of intestinal immune cells, related to Figure 1

(A) Experimental overview.

(B) Depletion of common cell types by FACS. Shown are representative FACS plots for sorting lgD^{low} cells (left) or $CD3^{-}CD19^{-}$ cells (right) from PP and LP regions. $CD45^{-}$ cells were not included in LP.

(C) An LP and PP cell atlas. A 2D embedding as in **Figure 1B**, but showing separately only the 36,797 cells from PP regions (left) or the 21,270 cells from LP (right).

(D) Cluster quality measures. Top: Distribution of number of UMIs (*y* axis, $\log_{10}$-transformed) in both LP and PP cells in each cluster from **Figure 1B** (x axis). Bottom: distribution of doublet scores (y axis, **STAR Methods**) of only PP cells in each cluster from **Figure 1B** (x axis).

(E) Clusters of specific cell types in the atlas. A 2D embedding as in **Figure 1B**, but showing separately only the cells in each cell lineage or group as labeled.

(F) Differentially expressed genes between ILC3 and LTi. Fraction of cells in the cluster that express a gene (dot size) and the z-score of the mean expression of that gene in those cells that express it in the cluster (color; z-score of average $\log_2(TPM+1)$).

(G) Tissue distribution of B (left) and T (right) cells between LP and PP in homeostasis. Proportion (*y* axis) of each cell type (*x* axis) in LP (red) and PP (black) regions. Points:

independent experiments; Box-and-whisker plots show the median, quartiles, and range. *p < 6×10^{-05}, **p < 4×10^{-10}, ***p < 2.5×10^{-153}, Wald test.

(H) Differential distribution of plasma cells and GC B cells. Representative IF image of the small intestines of wild type mice. White dashed line: PP region; Green dashed line: GC area; arrow: $CD138^{+}$ plasma cell; scale bar, 100 μm. Data are representative of three mice.

Figure S2. Cell proportions in T and B cells, and gene expression in ILC2s, mast cells, macrophages and plasma cells in OVA-induced type 2 inflammation, related to Figure 2

(A) Distribution of cell type proportions (y axis) in B cells (left) and T cells in homeostatic (black) or inflammatory (red) conditions. Points: independent experiments. Box-and-whisker plots show the median, quartiles, and range.

(B) Differentially expressed genes in ILC2s, mast cells, macrophages and plasma cells. Shown are genes repressed (blue) or induced (red) (|fold change| ≥ 2, FDR < 0.05, likelihood ratio test, frequency of expressing cells ≥ 25% at the up-regulation side) by the inflammation in each labeled cell type. Dots: genes, with key ones labeled.

(C) Distribution of expression levels (y axis, $\log_2$(TPM+1)) of *Igh* genes (labeled) in plasma cells in homeostatic (black) or inflammatory (red) conditions. *p < 2.8×10^{-5}, **p < 2.9×10^{-13}, ***p < 1.5×10^{-107}, likelihood ratio test.

Figure S3. Topic modeling on T cells, B cells, DCs, ILCs, myeloid cells and stromal cells, and co-expression of CCL21 and IL-33 in PDPN$^+$ stromal cells in the small intestine, related to Figure 3

(A-F) Biological programs in each cell subset revealed by topic modeling. Shown are topics in T cells (A), B cells (B), ILCs (C), myeloid cells (D), DCs (E) and stromal cells (F). Top (A-D) and left (E and F): a portion of the 2D embedding in **Figure 1B**, showing only cells from the noted subset cells, colored by the topic's weight in the cell. Bottom (A-D) and right (E and F): empirical cumulative density function (y axis) of topic weights (x axis) for cells from mice treated with PBS (black curve) or OVA (red curve). p values: Mann–Whitney U test.

(G) co-localization of CCL21 and IL-33 in subsets of PDPN$^+$ stromal cells (arrow) in the small intestines. Representative IF images of the small intestines of wild type mice. Scale bars, 50 μm. Data are representative of three mice.

Figure S4. Expression of *Calca, Calcrl, Ramp1* and *Il5* genes in intestinal KLRG1$^+$ ILC2s in homeostatic and inflammatory conditions, related to Figure 4

(A) Distribution of expression levels (y axis, $\log_2$(TPM+1)) of *Calca* (top), *Calcrl* (middle), *Ramp1* (bottom) in each cell types (*x* axis) in mice treated with PBS (black) or OVA (red). ILC2s are highlighted. $*P < 0.05$, $**P < 2.3\times10^{-06}$, likelihood ratio test.

(B) Expression level (y axis, Quantitative PCR normalized to *Gapdh*) of CT exon of *Calca*

gene in intestinal KLRG1$^+$ ILC2s isolated from PBS or OVA-treated mice. Points: individual experiment; mean and SEM, NS: p > 0.05, Student's *t* test.

(C) α-CGRP promotes *Il5* expression in intestinal ILC2s. Shown are Z scores of *Il5* gene in **Figure 4C**. Points: individual sample; mean and SEM, **FDR* < 0.05, ***FDR* < 0.01, ****FDR* < 0.001, Student's *t* test.

Figure S5. α-CGRP suppress expansion of intestinal KLRG1$^+$ ILC2s in two *in vivo* models, related to Figure 5

(A) α-CGRP co-treatment antagonizes CD3$^-$KLRG1$^+$ ILC2 expansion *in vivo*. Representative IF images of CD3$^-$KLRG1$^+$ ILC2 (arrows) in small intestines of mice treated as in **Figure 5A**. Scale bars, 200 μm. Data are representative of three mice in each condition.

(B) α-CGRP suppresses the expansion of ST2$^-$KLRG1$^+$ ILC2s in mLNs. Quantification of frequency (*y* axis) of ST2$^-$KLRG1$^+$ ILC2s in **Figure 5C**. Points: individual mice. Data from three independent experiments. mean and SEM, *FDR < 0.05, ***FDR < 0.001, Student's *t* test.

(C, D) α-CGRP treatment antagonizes intestinal ILC2 expansion in OVA-induced inflammation model. (C) Flow cytometry analysis of ILC2s (gated on CD45$^+$Lin$^-$ CD90.2$^+$IL7R$^+$) in the small intestines in mice treated as in **Figure 5F**. (D) Percent of GATA3$^+$ ILC2 (*y* axis) in all ILCs in the small intestine of mice in (C). Points: individual mice. Data

from three independent experiments. mean and SEM, **p < 0.01, Student's *t* test.

Figure S6. scRNA-seq analysis of intestinal epithelium and enteric neurons, and ATAC-seq analysis of intestinal ILC2s , related to Figure 6

(A) Undetectable expression of *Calca* and *Calcrl* in epithelium of wild type mice (Haber et al, 2017). Distribution of expression levels (y axis, $\log_2$(TPM+1)) of *Calca* (top), *Ramp1* (middle), *Calcrl* (bottom) in each epithelial cell type as labeled.

(B) Marker genes of each enteric neuron clusters. Heatmap showing relative expression (Z score of $\log_2$(TPM+1)) of top 5 marker genes (row) of each cluster (column) in **Figure 6A**.

(C) Distribution of expression levels (y axis, $\log_2$(TPM+1)) of *Chat*, *Gal*, *Il13ra1*, *Il4ra* and *Tslp* gene in each cluster (*x* axis) in **Figure 6A.**

(D) Interaction between ChAT-expressing neuron fibers and $CD3^{-}KLRG1^{+}$ ILC2s (arrow) in the small intestines. Representative IF images of the small intestines of wild type mice. Scale bar, 25 μm. Data are representative of three mice.

Supplementary information

Table S1. Differential expression analysis between the cells in each cluster and the remaining cells in PP regions, **related to Figure 1**

Table S2. Differential expression analysis between pairs of clusters in PP regions, **related to Figure 1**

Table S3. Differential expression analysis between cells from mice treated with OVA or PBS in each cell type in PP and LP regions, **related to Figure 2**

Table S4. Top 50 genes in each topics revealed by topic modeling on T cells, B cells, DCs, myeloid cells and stromal cells in PP and LP regions, **related to Figure 3**

Table S5. The enriched peaks and their associated genes in the intestinal KLRG1^{+} ILC2s stimulated *in vitro* with α-CGRP or control, **related to Figure 6**

STAR*METHOD

KEY RESOURCES TABLE

REAGENT or RESOURCE	SOURCE	IDENTIFIER
Antibodies		
rat anti-CD16/CD32 (2.4G2)	BD Biosciences	Cat# 553141, RRID:AB_394656
armenian hamster anti-CD3ε (145-2C11), APC	BioLegend	Cat# 100312, RRID:AB_312677
rat anti-CD5 (53-7.3), APC	BioLegend	Cat# 100626, RRID:AB_2563929
rat anti-CD19 (6D5), APC	BioLegend	Cat# 115512, RRID:AB_313647
rat anti-CD11b (M1/70), APC	BioLegend	Cat# 101212, RRID:AB_312795
rat anti-CD8 (53-6.7), APC	BioLegend	Cat# 100712, RRID:AB_312751
armenian hamster anti-CD11c (N418), APC	BioLegend	Cat# 117310, RRID:AB_313779
rat anti-Gr-1 (RB6-8C5), APC	BioLegend	Cat# 108412, RRID:AB_313377
armenian hamster anti-TCRγδ (eBioGL3), APC	Thermo Fisher Scientific	Cat# 17-5711-82, RRID:AB_842756
rat anti-CD170 (1RNM44N), eFluor 660	Thermo Fisher Scientific	Cat# 50-1702-80, RRID:AB_2574186
syrian hamster anti-KLRG1 (2F1), FITC	BioLegend	Cat# 138410, RRID:AB_10643582
rat anti-CD45 (30-F11), Alexa Fluor 594	BioLegend	Cat# 103128, RRID:AB_493715
rat anti-CD127 (A7R34), PE/CY7	BioLegend	Cat# 135014, RRID:AB_1937265
rat anti-CCR6 (29-2L17), BV421	BD Biosciences	Cat# 564736, RRID:AB_2738926
armenian hamster anti-TCRβ (H57-597), APC	Thermo Fisher Scientific	Cat# 17-5961-82, RRID:AB_469481
rat anti-NKp46 (29A1.4), PerCP/Cyanine5.5	BioLegend	Cat# 137609, RRID:AB_10642684
rat anti-CD90.2 (53-2.1), Brilliant Violet 605	BioLegend	Cat# 105343, RRID:AB_2632889
armenian hamster anti-FcεRI (Mar-1), Alexa Fluor 488	BioLegend	Cat# 134330, RRID:AB_2687239

rat anti-IgD (11-26c.2a), Alexa Fluor 594	BioLegend	Cat# 405740, RRID:AB_2565572
rat anti-GATA-3 (TWAJ), Alexa Fluor 488	Thermo Fisher Scientific	Cat# 53-9966-42, RRID:AB_2574493
rat anti-RORγt (B2D), PE	Thermo Fisher Scientific	Cat# 12-6981-82, RRID:AB_10807092
rat anti-IgD (11-26c.2a), Alexa Fluor 647	BioLegend	Cat# 405708, RRID:AB_893528
rat anti-IgD (11-26.2a), Alexa Fluor 594	BioLegend	Cat# 405740, RRID:AB_2565572
rat anti-CD138 (281-2), Alexa Fluor 647	BioLegend	Cat# 142525, RRID:AB_2566238
rat anti-GL7 (GL7), Alexa Fluor 488	Thermo Fisher Scientific	Cat# 53-5902-82, RRID:AB_2016717
rat anti-CD326 (EpCAM), eFluor 450	Thermo Fisher Scientific	Cat# 48-5791-82, RRID:AB_10717090
syrian hamster anti-CD3ε (17A2), Alexa Fluor 594	BioLegend	Cat# 152317, RRID:AB_2715809
rat anti-Podoplanin (eBio8.1.1), Alexa Fluor 488	BioLegend	Cat# 337005, RRID:AB_2161952
rat anti-CCL21/6Ckine (59106)	R&D Systems	Cat# MAB457, RRID:AB_2259799
goat anti-IL-33	R&D Systems	Cat# AF3626, RRID:AB_884269
syrian hamster anti-KLRG1 (2F1)	BD Biosciences	Cat# 562190, RRID:AB_11154418
rat anti-CGRP	Sigma-Aldrich	Cat# C8198, RRID:AB_259091
rabbit anti-DCAMKL1	Abcam	Cat# ab31704, RRID:AB_873537
donkey anti-goat IgG, Alexa Fluor 647	Thermo Fisher Scientific	Cat# A-21447, RRID:AB_2535864
donkey Anti-Rat IgG, Cy3	Jackson ImmunoResearch	Cat# 712-166-153, RRID:AB_2340669
goat anti-syrian hamster IgG, Alexa Fluor 488	Jackson ImmunoResearch	Cat# 107-546-142, RRID:AB_2337479
goat anti-rabbit IgG, Alexa Fluor 647	Jackson ImmunoResearch	Cat# 111-606-144, RRID:AB_2338083
rat anti-T1/ST2 (DJ8), PE	mdbioproducts	Cat# 101001PE
goat anti-ChAT	Sigma-Aldrich	Cat# AB144P
Chemicals, Peptides, Recombinant Proteins and Kits		
DAPI	Sigma-Aldrich	Cat# D9542

7-AAD	BD Biosciences	Cat# 559925
Fixable Viability Dye eFluor 780	Thermo Fisher Scientific	Cat# 65-0865-14
UltraPure 0.5M EDTA, pH 8.0	Thermo Fisher Scientific	Cat# 15575020
Ovalbumin	Sigma-Aldrich	Cat# A5503
aluminum potassium sulfate dodecahydrate	Sigma-Aldrich	Cat# A7210-500G
α-CGRP	AnaSpec	Cat# AS-20681
Recombinant Mouse IL-17E Protein	R&D Systems	Cat# 1399-IL-025
DNase I, grade II, from bovine pancreas	Sigma-Aldrich	Cat# 10104159001
RPMI-1640	Thermo Fisher Scientific	Cat# 72400-047
Liberase™ TM	Sigma-Aldrich	Cat# 5401127001
Percoll Plus	Sigma-Aldrich	Cat# GE17-5445-01
10X Chromium Single Cell 3' Kit	10X Genomics	Cat#120237
PicoPure RNA Isolation Kit	Thermo Fisher Scientific	Cat# KIT0204
iScript™ cDNA Synthesis Kit	Bio-Rad	Cat# 1708891
iTaq™ Universal SYBR® Green Supermix	Bio-Rad	Cat# 1725121
Recombinant Mouse IL-2 Protein	R&D Systems	Cat# 402-ML-020
Recombinant Mouse IL-7 Protein	R&D Systems	Cat# 407-ML-025
CellTrace Violet Cell Proliferation Kit	Thermo Fisher Scientific	Cat# C34557
O.C.T. Compound	Electron Microscopy Sciences	Cat# 62550-01
Triton X-100	Sigma-Aldrich	Cat# T8787
Normal Donkey Serum	Jackson ImmunoResearch	Cat# 017-000-001, RRID:AB_2337254
ProlongGold Antifade reagent	Thermo Fisher Scientific	Cat# P36930
TCL buffer (QIAGEN)	Qiagen	Cat# 1031576
2-Mercaptoethanol	Sigma-Aldrich	Cat# M6250
Gibco 2-Mercaptoethanol	Thermo Fisher Scientific	Cat# 21985023
Penicillin Streptomycin	Thermo Fisher Scientific	Cat# 15070063
Sodium Pyruvate	Thermo Fisher Scientific	Cat# 11360070

Nextera XT Sample Preparation Kit	Illumina	Cat#FC-131-1096
forskolin	STEMCELL technologies	Cat#72112
Deposited Data		
RNA-seq data	This paper	GEO: GSE124880
Experimental Models: Strains		
Mouse: BALB/cJ	Jackson Laboratory	Cat# JAX:000651, RRID:IMSR_JAX:000651
Mouse: B6.129S6-Calca<tm1Hku>	Brigham and Women's Hospital	Cat# RBRC04109, RRID:IMSR_RBRC04109
Oligonucleotides		
Reverse Transcription DNA oligonucleotide primer (RNase-free, 100 mM)	IDT	5'-AAGCAGTGGTATCAACGCAGAGTACT(30)VN-3'
SMARTER TSO (with LNA)	Exiqon	5'-AAGCAGTGGTATCAACGCAGAGTACrGrG+G-3'
PCR oligonucleotide primer	IDT	5'-AAGCAGTGGTATCAACGCAGAGT-3'
Calcrl-F	Sigma-Aldrich	5'-GCGTGAACCAAACAGACTTG-3'
Calcrl-R	Sigma-Aldrich	5'-TCATTCCAGCATAGCCATCC-3'
Ramp1-F	Sigma-Aldrich	5'-GGCTCTGCTTGCCATGG-3'
Ramp1-R	Sigma-Aldrich	5'-CCTTGAAGCGGCTGAGG-3'
Calca-F	Sigma-Aldrich	5'-TGCAGATGAAAGCCAGGG-3'
Calca-R-exon 5	Sigma-Aldrich	5'-CTTCACCACACCTCCTGATC-3'
Calca-R-exon 4	Sigma-Aldrich	5'-TGTTGAGGTCTTGTGTGTACG-3'
Calcr-F	Sigma-Aldrich	5'-CTACTTCTGGATGCTCTGCG-3'
Calcr-R	Sigma-Aldrich	5'-AGTGATGGCGTGGATAATGG-3'
Gapdh-F	Sigma-Aldrich	5'-CTTTGTCAAGCTCATTTCCTGG-3'
Gapdh-R	Sigma-Aldrich	5'-TCTTGCTCAGTGTCCTTGC-3'
Software and Algorithms		
ImageJ	(Schneider et al., 2012)	https://imagej.nih.gov/ij/
GraphPad Prism	GraphPad Software	https://www.graphpad.com/scientific-software/prism/

FlowJo	TreeStar	https://www.flowjo.com/solutions/flowjo
Bowtie	(Langmead et al., 2009)	http://bowtie-bio.sourceforge.net/index.shtml
10x cellranger	10X Genomics	https://support.10xgenomics.com/single-cell/ software/overview/welcome
RSEM	(Li and Dewey, 2011)	http://deweylab.github.io/RSEM/
edgeR	(Robinson et al., 2010)	https://gist.github.com/jdblischak/11384914
code for single-cell RNA-seq analysis	This paper	https://bitbucket.org/jerry00/mouse_small_intestine_immune_cell_atlas/src/master/

EXPERIMENTAL METHODS

Mice

BALB/cJ mice (Jax 000651) were obtained from the Jackson Laboratory. α-CGRP knock out mice (B6.129S6-Calca<tm1Hku>) were kindly provided by Dr. Vijay K. Kuchroo (Brigham and Women's Hospital, Boston, Massachusetts, USA). Mice were housed in specific pathogen-free conditions and were used and maintained in accordance with the Institutional Animal Care and Use Committee (IACUC) protocol # 0055-05-15.

To induce allergic reaction to OVA, 6 to 7 weeks old mice were sensitized twice, two weeks apart, with 50 μg of OVA plus 1 mg of aluminum potassium sulfate adjuvant via intraperitoneal injection. Two weeks later, mice were orally administered with 50 mg of OVA on every other day for a total of five times. 1 μg of α-CGRP peptide was administered simultaneously when indicated. Mice were deprived of food for 3–4 hours in cages with wood

chip bedding for limiting antigen degradation in the stomach before each intragastric challenge.

To activate ILC2s *in vivo*, 200 ng of IL-25 was intraperitoneally injected into 7-10 weeks old mice daily for two days. 1 μg α-CGRP was injected together as noted.

Isolation of cells from Peyer's patches (PPs)

Peyer's patches (PPs) were carefully dissected from the small intestine under a stereo microscope using a fine scissor, pierced once with a fine forcep. Tissues were digested in freshly made digestion buffer (RPMI-1640 containing 100 μg/ml Liberase TM and 50 μg/ml DNase I at 37°C on a roto-mixer. After 15 min, tissues were very gently mixed using a 1 ml pipette. The supernatant was collected and added to ice-cold MACS buffer (pH 7.4; PBS plus 2% FCS and 2mM EDTA). Pre-warmed (37°C) fresh digestion buffer was added to the remaining tissues. After rotation at 37°C for 15 min, the mixture was vigorously mixed using a 1ml pipette for 1 min. Supernatants from the two steps were combined and passed through 70 μm filters and stained for FACS (below).

Isolation of cells from the lamina propria (LP)

The small intestines were opened longitudinally and washed in ice-cold PBS. For scRNA-seq,

roughly 0.5 cm of fragments from each of the distal, middle and proximal regions without visible PPs were collected. Epithelial cells were dissociated by tissue rotation in pre-warmed (37°C) PBS containing 10 mM EDTA at 37°C for 15 min, followed by additional incubation on ice for 15 min. Tissues were then shaken vigorously. After washing twice with PBS containing 2% FCS, tissues were digested in pre-warned (37°C) digestion buffer at 37°C on a roto-mixer for 25 min. The supernatants were then passed through 70 μm filters and stained for FACS.

For experiments other than scRNA-seq, the entire small intestine was cut into 1 cm pieces after eliminating PPs. Epithelial cells dissociation was performed by stirring tissues in flasks containing PBS and 10 mM EDTA on a magnetic stirrer at 37°C two times for 15 min. After vortex, the tissue was stirred in pre-warmed (37°C) digestion buffer for 25 min at 37°C. The supernatant was passed through 100 μm filter. Leukocytes were further enriched by a 40%/70% Percoll gradient centrifugation before flow staining.

Flow cytometry and cell sorting

Cells were washed and suspended in MACS buffer (pH 7.4; PBS plus 2% FCS and 2 mM EDTA). Nonspecific antibody binding was blocked with CD16/CD32 (2.4G2) antibody for 15 min on ice. Cells were then stained with antibody cocktails for 30 min at 4°C. Lineage-positive cells were excluded for analyzing ILCs by staining for CD3ε (145-2C11), CD5 (53-7.3), CD19

(6D5), CD11b (M1/70), CD8 (53-6.7), CD11c (N418), Gr-1 (RB6-8C5), TCRγδ (eBioGL3 (GL-3, GL3)) and TCRβ (H57-597). To analyze mast cells, lineage-positive cells were excluded by staining for CD3ε, CD5, CD19, CD11c and SiglecF (E50-2440). For surface staining, antibodies for KLRG1 (2F1), CD45 (30-F11), CD127 (A7R34), CCR6 (29-2L17), NKp46 (29A1.4), CD90.2 (53-2.1), FcεRI (Mar-1), IgD (11-26c.2a) and ST2 (DJ8) were used. For intracellular staining, cells were fixed and permeabilized using the Foxp3 transcription factor staining buffer set, followed by staining with anti-GATA-3 (TWAJ) or anti-RORγt (B2D) antibodies. Dead cells were excluded with 7-AAD or Fixable Viability Dye eFluor 780. Flow cytometry was performed on Cytoflex (Beckman Coulter) and analyzed with FlowJo software. Sorting was performed with the SH800S Cell Sorter (Sony Biotechnology).

Droplet-based scRNA-seq

Single cells were captured via the GemCode Single Cell Platform using the GemCode Gel Bead, Chip and Library Kits (10X Genomics), according to the manufacturer's protocol. Briefly, flow-sorted cells were suspended in PBS containing 0.4% BSA, and loaded at 7,000 cells per channel. The cells were then partitioned into GemCode instrument, where individual cells were lysed and mixed with beads carrying unique barcodes in individual oil droplets. The products were subjected to reverse transcription, emulsion breaking, cDNA amplification,

shearing, 5′ adaptor and sample index attachment. Libraries were sequenced on a HiSeq 2500 (Illumina).

Quantitative real-time PCR

RNA was isolated from 10,000 cells per sample using PicoPure RNA Isolation Kit, according to the manufacturer's protocol and reverse transcribed to cDNA with iScript cDNA Synthesis Kit. Gene expression was analyzed by quantitative real-time PCR on a ViiA7 System (Thermo Fisher Scientific) using iTaq™ Universal SYBR® Green Supermix with the primers listed in the KEY RESOURCES TABLE. Expression values were calculated relative to *Gapdh* detected in the same sample by qPCR.

ILC2 culture

Sort-purified intestinal KLRG1$^+$ ILC2s were incubated in RPMI supplemented with 10% FCS, 10mM Hepes, 1mM sodium pyruvate, 10% FBS, 80μm 2-mercaptoethanol, 2mM glutamine, 100U/ml penicillin, 100μg/ml streptomycin, 100 ng/ml IL-2 and 100 ng/ml IL-7 in 96-well round bottom plate at 37°C and 5% CO_2. If indicated, the culture was supplemented with 100 ng/ml IL-25. For the *in vitro* proliferation assay, cells from different mice were pooled and labeled with CellTrace Violet, and then cultured at 1,000-1,500 cells per well with 10 μg/ml α-

CGRP for 60 hours. When indicated, 10 μM forskolin or 1 μM SQ 22, 536 in DMSO was supplied and cells were cultured for 40 hours. For bulk RNA-seq, cells from individual mice were stimulated at 200 cells per well with 0.4 μg/ml α-CGRP for 3 hours. For bulk ATAC-seq, cells were stimulated with 0.4 μg/ml α-CGRP for 2 hours.

Immunofluorescence staining and imaging

The small intestines were fixed in 2% PFA, embedded in O.C.T. Compound and sliced into 10 μm by frozen section. The slides were blocked with 0.1% Triton X-100, 2% FCS and donkey serum. The staining reagents incudes Alexa Fluor 594 anti-IgD (11-26.2a), Alexa Fluor 647 anti-CD138 (281-2), eFluor 450 anti EPCAM (G8.8), Alexa Fluor 594 anti-CD3ε (17A2), Alexa Fluor 488 anti-Podoplanin (eBio8.1.1 (8.1.1)), rat anti-CCL21/6 (59106), goat anti-IL-33 (polyclonal), hamster anti-KLRG1 (2F1), rat anti-CGRP (polyclonal), goat anti-ChAT (polyclonal), rabbit anti-DCAMKL1 (polyclonal), Alexa Fluor 647-donkey anti-goat IgG, Alexa Fluor 647 donkey anti-goat IgG, Cy™3 donkey anti-rat IgG, Alexa Fluor 488 goat anti-syrian hamster IgG (H+L), Alexa Fluor 647 goat anti-rabbit IgG (H+L) and DAPI. Slides were mounted with the ProlongGold Antifade reagent and examined with a ZEISS LSM 710 upright microscope using×10, ×20 air or ×60 oil immersion lens. The images were analyzed with ImageJ.

Bulk RNA-seq

200 ILC2s from each condition were lysed in 10 ul TCL buffer plus 0.5% 2-Mercaptoethanol. Libraries were processed with SMART-Seq2 (Picelli et al., 2013) with at least three replicates per condition, and paired-end sequenced (75 bp × 2) with a 75 cycle Nextseq 500 high output V2 kit.

Reads were aligned to the mouse reference genome (NCBI 38, mm10) using Bowtie (Langmead et al., 2009) with default parameters, and expression abundances were estimated using RSEM software (Li and Dewey, 2011). The differential gene expression analysis was performed with edgeR (Robinson et al., 2010) with default parameters.

Bulk ATAC-seq

ATAC-seq experiment was performed using a published protocol (Buenrostro et al., 2013) with minor modifications. Briefly, 2, 000 cells in 5 μl PBS, 17.3 μl H_2O and 25 μl of transposition buffer (66 mM Tris-acetate, 132 mM K-acetate, 20 mM Mg-acetate, 32% DMF, and 0.2% NP-40) were mixed and incubated at room temperature for 10 min. After adding 2.5 μl of Tn5

transposase to the reaction, the transposition was carried out at 37°C for 30 min with gentle shaking at 300 rpm and then purified with Zymo DNA Clean and Concentrator (Zymo Research). The library was amplified for 11 cycles, purified with Zymo DNA clean (Zymo Research), and sequenced on an Illumina Next-seq platform using 75 cycle Nextseq 500 high output V2 kit (Read 1: 38 cycles, Index 1: 8 cycles, Index 2: 8 cycles, Read 2: 38 cycles).

The reads were trimmed and aligned to the mouse reference genome (mm9) with Bowtie2 aligner (Langmead and Salzberg, 2012) using the option -X2000. Then, we discarded reads with alignment quality < Q30, improperly paired, mapped to the unmapped contigs, chrY, and mitochondria. Duplicates were removed using Picard tools (function MarkDuplicates, http://broadinstitute.github.io/picard/). MACSv2 peak caller (Zhang et al., 2008) (version: 2.1.1) was used to call accessible regions of open chromatin regions (ATAC-Seq peaks) with the following parameters (--nomodel –nolambda –keep-dup -call-summits). Peaks overlapping with ENCODE blacklisted regions were filtered out using BEDtools (function itersectBed). Peak summits were extended by ±250 bp, and fragment counts in peaks were calculated using chromVAR (Schep et al., 2017) (version: 1.1.1). Peaks were allocated to genes using GREAT (McLean et al., 2010) (version: 3.0.0) with "basal plus extension" association rule with default parameters. Functional enrichment analysis was performed using GREAT (version: 3.0.0).

COMPUTATIONAL METHODS

scRNA-seq data QC and pre-processing

Reads were aligned to the mouse reference genome (NCBI 38, mm10) using Cell Ranger v2.1.1 (10x Genomics) to generate cell-gene count matrices. After removing cells with less than 500 UMIs and high mitochondrial RNA UMIs (more than four times of the median number of mitochondrial UMIs across cells), we obtained 36,797 cells from PP regions (15,939 cells from OVA-allergic mice and 20,858 cells from controls), and 21,270 cells from LP (11,405 cells from OVA-allergic mice and 9,865 cells from controls). 19,221 genes were retained after filtering genes expressed in less than five cells.

We expected batch effects in the data, because libraries were prepared and sequenced at different times, and because we used two sorting strategies to remove either IgD^+ Naive B cells or CD19+/$CD3^+$ cells. Moreover, the number of recovered cells varied across experiments; for example, we recovered 10,567, 6,439, 5,016, 4,571, and 10,204 cells from each of the five experiments for cells from PPs. We explored several possibilities to address these confounders. Two recent methods have been developed to align scRNA-seq data from different batches (Butler et al., 2018; Haghverdi et al., 2018). However, a cell type must be shared by all datasets for Seurat's CCA approach to correctly align cells (Butler et al., 2018), which is not appropriate

for our case. mnnCorrect (Haghverdi et al., 2018) can merge datasets with private (distinct) cell types, but in our datasets where there were dozens of cell types, mnnCorrect successfully merged only some of these clusters, and failed to align cells from other clusters. (More recent methods (Korsunsky et al., 2018; Lin et al., 2018; Stuart et al., 2018; Welch et al., 2018) might help merge cells from different experiments but were published when this analysis was long completed.)

Principal Component Analysis (PCA) is typically used to extract a small number of features (principal components (PCs)) from a normalized gene-cell count matrix. These feature vectors were used for clustering analysis or as inputs for visualization. Unfortunately, in the presence of batch effects, some of the top features typically captured batch effects (Chen et al., 2011). Therefore, batch effects could not be removed by discarding the features with small eigenvalues in PCA.

To help address these batch effects, we took an alternative approach, where we projected the scRNA-seq data to a reference dataset consisting of microarray measurements of immune cells from 276 samples (Heng et al., 2008). Specifically, we first did PCA on the microarray data and extracted the first 101 eigenvectors. We discarded the first eigenvector as the corresponding first PC was correlated with batch information in the microarray data. We next

projected the scRNA-seq data to the 100-dimensional space spanned by the eigenvectors (PCs 2-101) from the microarray data. The coordinates of cells in the 100-dimensional space were used for clustering and as inputs of scvis.

scRNA-seq clustering of PP cells

We used the Louvain community detection algorithm (Blondel et al., 2008; Levine et al., 2015) to cluster cells from Peyer's patch regions. As the Louvain clustering algorithm tends to miss some small clusters, we used densityCut (Ding et al., 2016) to find the likely cluster centers. For each center, we changed the edge weights (w′) connecting the cluster center to its neighbors to (w′) = 2*kw*, where *k* is the number of nearest neighbors in the *k*-nearest neighbor (*k*-NN) graph, and *w* is the original edge weight of an edge. Louvain clustering on this edge re-weighed graph produced 46 clusters.

Next, we assessed the robustness of the cell to cluster assignment. For each cluster and each batch, we computed the 'bulk' gene expression profile of the cells from a given batch in the cluster. The 'bulk' gene expression profile for a set of cells is computed by first taking the sum of the gene expression vectors from these cells, where the gene expression vector of a cell was the raw UMI count vector, one element for a gene. The dimensionality of a gene expression

vector was the number of genes. To make the bulk gene expression vectors from different sets of cells comparable, a bulk gene expression vector was normalized by dividing the total number of UMIs from all the cells used in computing that bulk gene expression vector, and further multiplying by 10^4 and finally taking the log transform (adding one before the log transformation to make all the elements of the bulk vector positive). Then, for each cell, we computed its Pearson correlation coefficient with the "bulk" profile for each cluster. We denote the maximum correlation between a cell x and the bulk profiles of cluster i (from different batches) as c_i. If cell x is originally assigned to cluster j, and $c_j < 0.9c_k$, then we reassign cell x to cluster k. Only ~0.26% (97 of 36,797) cells were re-assigned to clusters different from their original assignment. We also tested whether two clusters should be merged, if there are no more than 10 significantly differentially expressed genes between them (with differential expression estimated with the Wilcoxon rank-sum test in the package Seurat (Butler et al., 2018)). However, none of the 46 clusters required merging by this criterion.

Clustering cross-validation of PP cells

We performed a 10-fold cross validation analysis on the PP data to evaluate the quality of the clustering. We partitioned the PP data into ten approximately equal size sets, and trained a *k*-nearest neighbor (*k*-NN) classifier (we used a small $k = 11$ as some clusters are small, *e.g.*, 17

cells in cluster 46) on nine folds of data, leaving one fold of data for testing. We repeated this training and testing scheme ten times such that all the data points were used for testing only once.

The *k*-NN classifiers had a high overall accuracy of 97.2%. Classification accuracy varied for cells from different clusters, with those from cluster 39 having the lowest accuracy of 65.6%. Cluster 39 consisted of a mixture of low-quality plasma B cells and cell doublets (macrophage and epithelial cell doublets). A subgroup of cells expressed plasma B cell marker genes, such as *Jchain* and *Mzb1*, but had a relatively small number of UMIs per cell compared to the cells from the plasma cell Cluster 20 (**Figure S1D**). Some of these low-quality plasma B cells also had high mitochondrial UMI ratios. Another subset of cells in Cluster 39 expressed both epithelial cell markers (*e.g.*, *Epcam* and *Krt8*) and macrophage marker genes (*e.g.*, Lyz1 and Lyz2). These cells had a very large number of UMIs per cell (**Figure S1D**) and likely represented potential macrophage and epithelial cell doublets. Notably, although the number of cells in each cluster was extremely unbalanced (*e.g.*, 6,948 cells in cluster 1 but only 17 cells in cluster 46), the classification accuracies were largely uncorrelated with the number of cells in each cluster.

Cluster annotation and filtering of PP cells

We next used MAST (Finak et al., 2015) to identify significantly up-regulated marker genes for each of the 46 clusters, accounting for batch (experimental dates) and the scaled number of detected genes in each cell as covariants (Soneson and Robinson, 2018). Based on known function of the marker genes, we annotated 6 major cell lineages/groups: T cells, B cells, dendritic cells, ILCs, myeloid cells and stromal cells.

We conservatively excluded from further analyses the smallest clusters (<0.05% of all cells) and several ambiguous clusters that we could not confidently assign with cell identities. We note that the small clusters may be biologically valid, but the small number of cells limits our ability to further study them here. For example, the top markers of cluster 45 (18 cells) included *Dntt*, *Rag1*, *Chrna9*, *Tctex1d1*, *Arpp21*, which are highly expressed in progenitors of T cells at the double-positive stage in Immgen (Heng et al., 2008; Painter et al., 2011). Cluster 46 (17 cells) may consist of lymph node lymphatic endothelial cells, as they expressed their known marker genes such as *Lyve1*, *Prox1*, and *Cp*. Experimental validations are required for confidently including them in the downstream analyses. Cells in Cluster 34 (100 cells) from PP, expressed both pDC and myeloid gene markers. Only two marker genes (*Gtf2a1* and *2310001H17Rik*) overlapped between Cluster 34, and either of its adjacent clusters in scvis, clusters 6 and 22 (**Figure 1B**). *Gtf2a1* was expressed lowly in about 25% of the cluster 34 cells

and *2310001H17Rik* was expressed in several other cell types, such as T cells and neutrophils. We annotated cluster 34 as 'Unresolved'. Cluster 18 and cluster 37 were also annotated as 'Unresolved' based on similar analysis. Cluster 40 cells expressed macrophages marker gene like *Lyz2*. Compared to the macrophage cluster (cluster 22), cluster 40 cells expressed higher level of *C1qa*, *C1qb*, and *C1qc*. However, Cluster 40 cells had less UMIs per cells (**Figure S1D**) than Cluster 22 cells. We also labeled Cluster 40 as 'Unresolved'.

We further removed clusters enriched for doublets. To this end, we analyzed PP cells with Scrublet (Wolock et al., 2018), identifying clusters 29, 41, and 43 cells with high doublet scores, together accounting for 0.63% (232 of 36,797) of the PP cells. Cluster 42 cells also had high doublet scores, albeit lower than these other three clusters, and may be further potential doublets.

Clustering LP cells

We used the 35,691 PP cells that were both confidently assigned to clusters in the cross-validation above and had a *k*-NN probability greater than 0.5, to train a *k*-NN classifier (k = 11), and used it to classify the 21,270 LP cells. The vast majority of LP cells (97.4%, 20,724 / 21,270) were assigned to 42 of the 46 clusters with *k*-NN probability greater than 0.5. We

refined the clustering as done for the Peyer's patch data but only for the cells with *k*-NN probabilities less than 0.5. This reassigned only 0.12% (26 / 21,270) cells. 34 of the 42 clusters had >15 cells. To find potential LP-specific clusters (cell types that were only observed in LP), we concatenated the data from PPs and LP and then clustered the merged data. Of the clusters enriched in cells from LP (more than three times the number of cells from LP than PPs), two consisted of mast cells and three of plasma B cells. One of these clusters had cells with a low number of UMIs per cell without apparent marker genes. One LP-enriched cluster consisted of fibroblasts that expressed marker genes, such as *Col15a1*, *Ecm1*, and *Col6a5*.

Ten-fold cross validation of the 21,223 LP cells in 34 clusters with >15 cells showed 94.59% accuracy for all cells. Cells from three small clusters 5, 19, and 42 (32, 41, and 19 cells, respectively) had relatively low cross-validation accuracies of 0.41, 0.56, and 0.53, respectively. Overall, ~93.70% (19,886 / 21,223) were assigned robustly (correctly classified in cross-validation and with *k*-NN probabilities greater than 0.5).

Cellular composition changes

As different gating strategies (IgD^{low} or $CD3^{-}CD19^{-}$) directly influenced the frequencies of T and B cells, which subsequently affected the proportions of all other cell types, we separately quantified cell compositions in B cells, T cells, and other non-TB cell types. In addition, for

analyzing changes in the composition of B cell subsets, we did not include cells from the experiments with $CD3^{-}CD19^{-}$ sorting.

We used the negative binomial regression model with treatment (OVA or PBS) and spatial information (PP or LP) as covariates. The total number of analyzed cells (*e.g.*, the total number of T cells when quantifying T cells variations) from each experiment was used as an offset variable. The P value for the significance of treatment (OVA) on a cell type was assessed using the Wald test on the regression coefficient. We performed similar analyses to quantify cell composition changes between PPs and LP but only using cells in homeostasis. In addition, we used spatial information (PP or LP) as a covariate and the total number of analyzed cells from each experiment as an offset variable. The P value for the significance of location information (LP) on a cell type was also assessed using the Wald test on the regression coefficient.

Cell sampling frequencies

To estimate the number of required cells such that we have the power to recover rare cell types, we used the online tool: http://satijalab.org/howmanycells. The method assumes that the probability of observing at least N cells of a cell type in a sample of size K can be modeled by the cumulative distribution function of a negative binomial NBcdf(K; N, p), where p is the relative abundance of this cell type.

Topic modeling

To help guide LDA to find the informative topics, we learned multiple topic models for each subgroup of cells separately. (We had found that topic modeling of all subsets together mostly identifies cell type programs; data not shown.) Specifically, we used the FitGoM() function from the CountClust R package (Dey et al., 2017) to fit LDA topic models to the UMI counts (Bielecki et al., 2018) for cells belonging to each major identified cell type from the LP and PP regions. This resulted in 12 models, two for each of the following cell types: T cells (583 LP cells, 12,187 PP cells), DC cells (3,738 LP cells, 3,530 PP cells), B cells (5,648 LP cells, 7,376 cells), ILC cells (5,484 LP cells, 9,396 PP cells), myeloid cells (1,825 LP cells, 579 PP cells), and stromal cells (90 LP cells, 443 PP cells). Genes starting with 'Rpl' or 'Rps' were removed from the counts matrix prior to fitting the topic models, leaving a total of 19,108 genes included in each count matrix. The number of topics to fit and the tolerance value are required to run FitGoM() function. Thus, for each cell type and region, we fit a range of K and then used compGoM() to compute the Bayesian Information Criterion (BIC) the estimated likelihood, from which we calculated the Akaike Information Criterion (AIC). Our final choice of K value was primarily guided by the BIC curve; we aimed to choose a K at which the BIC was minimal, or decreasing less quickly. We set the tolerance value to 0.1. The top genes to highlight for each topic were selected using the ExtractTopFeatures() function.

Statistical analysis

Mice from which we failed to isolate a sufficient number of live cells for downstream analysis were excluded. Prism 7 (GraphPad Software) was used to perform two-tailed *t*-test and Fisher's exact test as indicated (except for RNA-seq data). P-values from multiple comparisons were adjusted in R.

Code availability

Code will be made available from bitbucket:

https://bitbucket.org/jerry00/mouse_small_intestine_immune_cell_atlas/src/master/

Data availability

The data are deposited in the Gene Expression Omnibus (GEO; GSE124880, https://www.ncbi.nlm.nih.gov/geo/query/acc.cgi?acc=GSE124880, enter token clczsgwmxhkptsl into the box), and the Single Cell Portal https://portals.broadinstitute.org/single_cell/study/fasi-immune-mouse-small-intestine.

References for Methods

Bielecki, P., Riesenfeld, S.J., Kowalczyk, M.S., Amezcua Vesely, M.C., Kroehling, L., Yaghoubi, P., Dionne, D., Jarret, A., Steach, H.R., McGee, H.M., *et al.* (2018). Skin inflammation driven by differentiation of quiescent tissue-resident ILCs into a spectrum of pathogenic effectors. bioRxiv.

Blondel, V.D., GuillaumeT, J., Lambiotte, R., and Lefebvre, E. (2008). Fast unfolding of communities in large networks. Journal of Statistical Mechanics: Theory and Experiment *2008*.
Buenrostro, J.D., Giresi, P.G., Zaba, L.C., Chang, H.Y., and Greenleaf, W.J. (2013). Transposition of native chromatin for fast and sensitive epigenomic profiling of open chromatin, DNA-binding proteins and nucleosome position. Nature methods *10*, 1213-1218.

Butler, A., Hoffman, P., Smibert, P., Papalexi, E., and Satija, R. (2018). Integrating single-cell transcriptomic data across different conditions, technologies, and species. Nat Biotechnol *36*, 411-420.

Chen, C., Grennan, K., Badner, J., Zhang, D., Gershon, E., Jin, L., and Liu, C. (2011). Removing batch effects in analysis of expression microarray data: an evaluation of six batch adjustment methods. PloS one *6*, e17238.

Dey, K.K., Hsiao, C.J., and Stephens, M. (2017). Visualizing the structure of RNA-seq expression data using grade of membership models. PLoS genetics *13*, e1006599.

Ding, J., Shah, S., and Condon, A. (2016). densityCut: an efficient and versatile topological approach for automatic clustering of biological data. Bioinformatics *32*, 2567-2576.

Finak, G., McDavid, A., Yajima, M., Deng, J., Gersuk, V., Shalek, A.K., Slichter, C.K., Miller, H.W., McElrath, M.J., Prlic, M., *et al.* (2015). MAST: a flexible statistical framework for assessing transcriptional changes and characterizing heterogeneity in single-cell RNA sequencing data. Genome Biol *16*, 278.

Haghverdi, L., Lun, A.T.L., Morgan, M.D., and Marioni, J.C. (2018). Batch effects in single-cell RNA-sequencing data are corrected by matching mutual nearest neighbors. Nat Biotechnol *36*, 421-427.

Heng, T.S., Painter, M.W., and Immunological Genome Project, C. (2008). The Immunological Genome Project: networks of gene expression in immune cells. Nature immunology *9*, 1091-1094.

Korsunsky, I., Fan, J., Slowikowski, K., Zhang, F., Wei, K., Baglaenko, Y., Brenner, M., Loh, P.-R., and Raychaudhuri, S. (2018). Fast, sensitive, and flexible integration of single cell data with Harmony. bioRxiv, 461954.

Langmead, B., and Salzberg, S.L. (2012). Fast gapped-read alignment with Bowtie 2. Nature methods *9*, 357-359.

Langmead, B., Trapnell, C., Pop, M., and Salzberg, S.L. (2009). Ultrafast and memory-efficient alignment of short DNA sequences to the human genome. Genome Biol *10*, R25.

Levine, J.H., Simonds, E.F., Bendall, S.C., Davis, K.L., Amir el, A.D., Tadmor, M.D., Litvin, O., Fienberg, H.G., Jager, A., Zunder, E.R., *et al.* (2015). Data-Driven Phenotypic Dissection of AML Reveals Progenitor-like Cells that Correlate with Prognosis. Cell *162*, 184-197.

Li, B., and Dewey, C.N. (2011). RSEM: accurate transcript quantification from RNA-Seq data with or without a reference genome. BMC Bioinformatics *12*, 323.

Lin, Y., Ghazanfar, S., Wang, K., Gagnon-Bartsch, J.A., Lo, K.K., Su, X., Han, Z.-G., Ormerod, J.T., Speed, T.P., Yang, P., *et al.* (2018). scMerge: Integration of multiple single-cell transcriptomics datasets leveraging stable expression and pseudo-replication. bioRxiv, 393280.

McLean, C.Y., Bristor, D., Hiller, M., Clarke, S.L., Schaar, B.T., Lowe, C.B., Wenger, A.M., and Bejerano, G. (2010). GREAT improves functional interpretation of cis-regulatory regions. Nat Biotechnol *28*, 495-501.

Painter, M.W., Davis, S., Hardy, R.R., Mathis, D., Benoist, C., and Immunological Genome Project, C. (2011). Transcriptomes of the B and T lineages compared by multiplatform microarray profiling. Journal of immunology *186*, 3047-3057.

Picelli, S., Bjorklund, A.K., Faridani, O.R., Sagasser, S., Winberg, G., and Sandberg, R. (2013). Smart-seq2 for sensitive full-length transcriptome profiling in single cells. Nature methods *10*, 1096-1098.

Robinson, M.D., McCarthy, D.J., and Smyth, G.K. (2010). edgeR: a Bioconductor package for differential expression analysis of digital gene expression data. Bioinformatics *26*, 139-140.
Schep, A.N., Wu, B., Buenrostro, J.D., and Greenleaf, W.J. (2017). chromVAR: inferring transcription-factor-associated accessibility from single-cell epigenomic data. Nature methods *14*, 975-978.

Schneider, C.A., Rasband, W.S., and Eliceiri, K.W. (2012). NIH Image to ImageJ: 25 years of image analysis. Nature methods *9*, 671-675.
Soneson, C., and Robinson, M.D. (2018). Bias, robustness and scalability in single-cell differential expression analysis. Nature methods *15*, 255-261.

Stuart, T., Butler, A., Hoffman, P., Hafemeister, C., Papalexi, E., Mauck, W.M., Stoeckius, M., Smibert, P., and Satija, R. (2018). Comprehensive integration of single cell data. bioRxiv, 460147.

Welch, J., Kozareva, V., Ferreira, A., Vanderburg, C., Martin, C., and Macosko, E. (2018). Integrative inference of brain cell similarities and differences from single-cell genomics. bioRxiv, 459891.

Wolock, S.L., Lopez, R., and Klein, A.M. (2018). Scrublet: computational identification of cell doublets in single-cell transcriptomic data. bioRxiv, 357368.

Zhang, Y., Liu, T., Meyer, C.A., Eeckhoute, J., Johnson, D.S., Bernstein, B.E., Nusbaum, C., Myers, R.M., Brown, M., Li, W., *et al.* (2008). Model-based analysis of ChIP-Seq (MACS). Genome Biol *9*, R137.

Figure 1

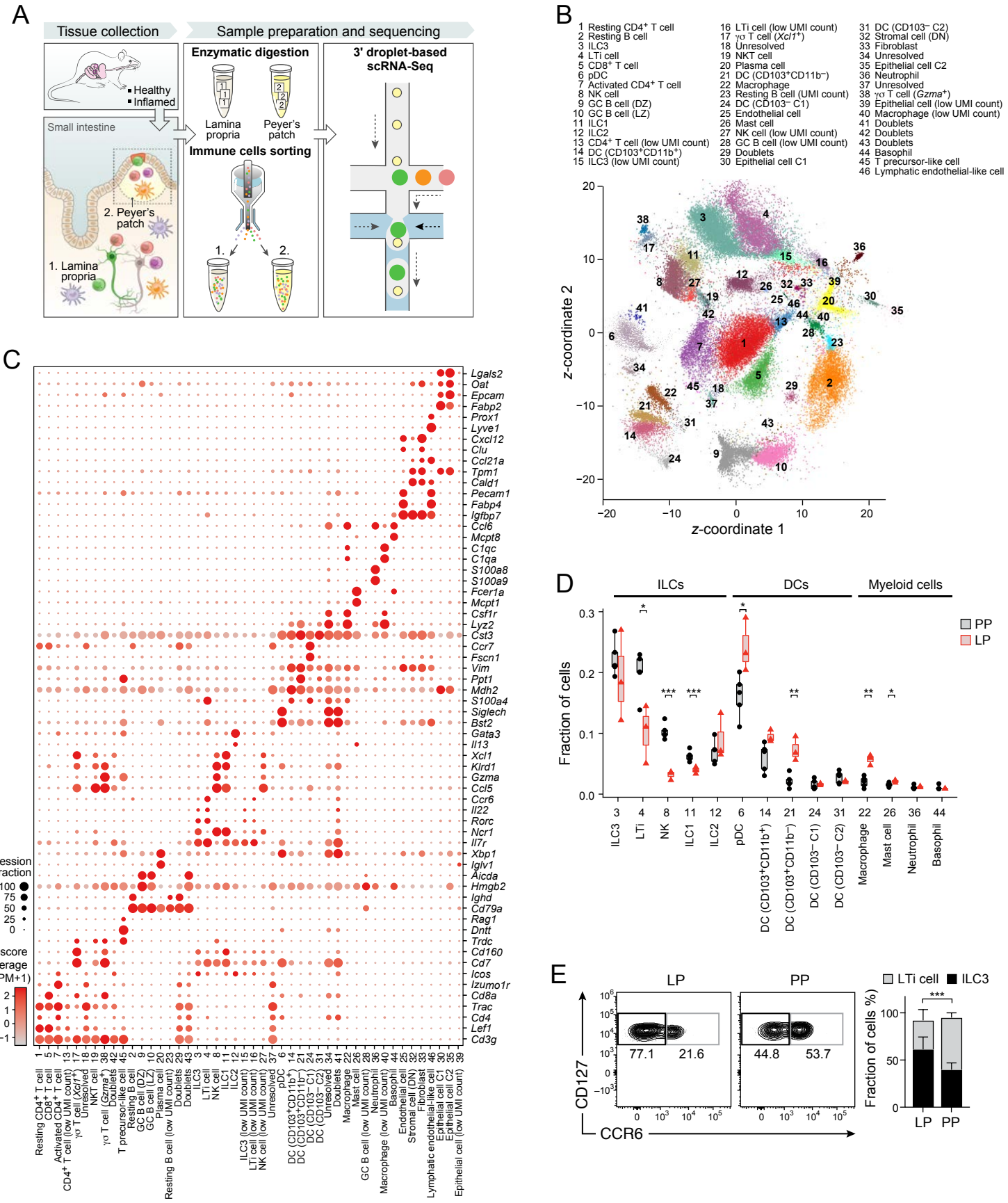

Figure 2

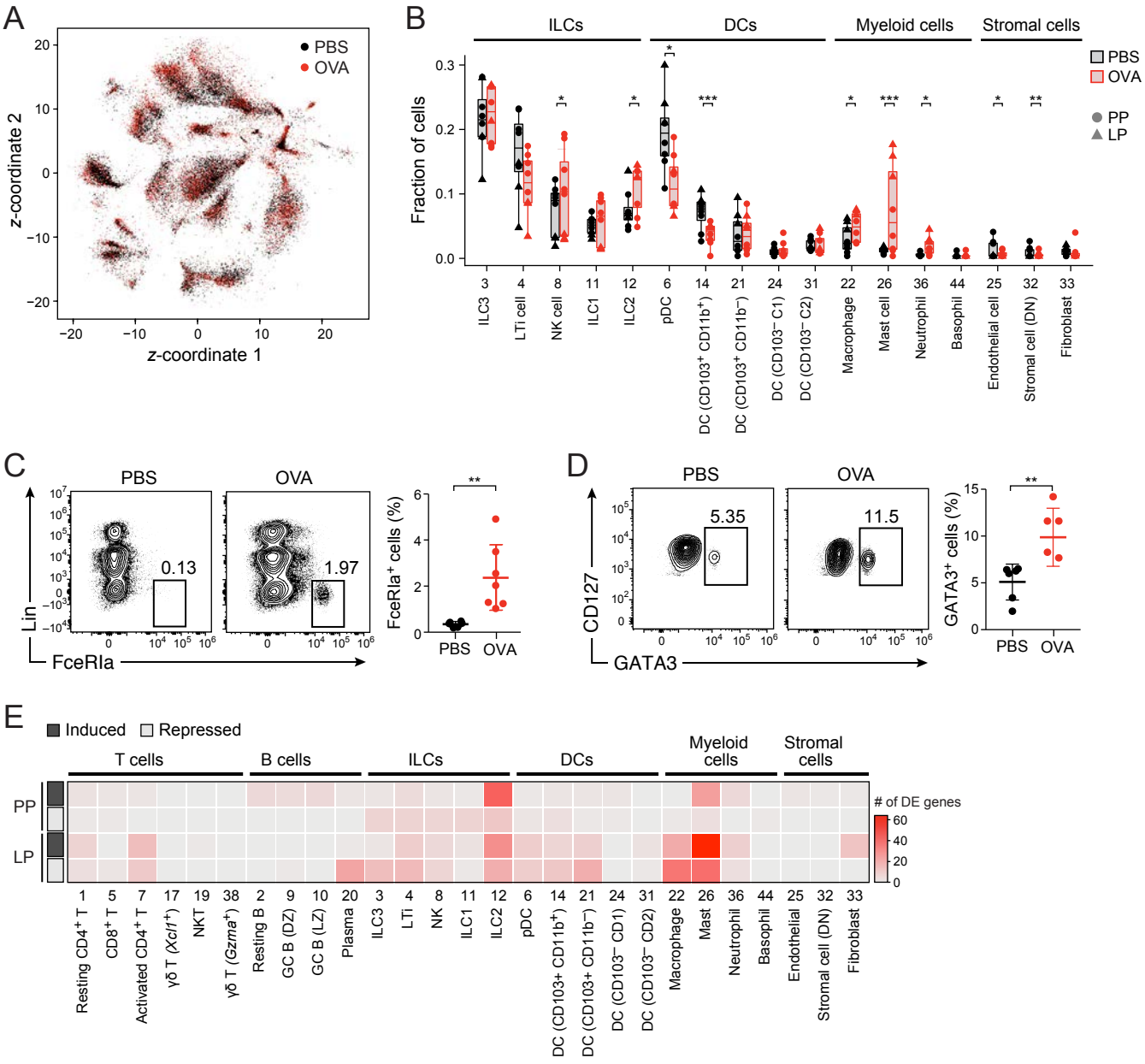
A
PBS
OVA
z-coordinate 2
z-coordinate 1
B
ILCs
DCs
Myeloid cells
Stromal cells
PBS
OVA
PP
LP
Fraction of cells
ILC3
LTi cell
NK cell
ILC1
ILC2
pDC
DC (CD103+ CD11b+)
DC (CD103+ CD11b−)
DC (CD103− C1)
DC (CD103− C2)
Macrophage
Mast cell
Neutrophil
Basophil
Endothelial cell
Stromal cell (DN)
Fibroblast
C
PBS
OVA
Lin
FceRIa
0.13
1.97
FceRIa+ cells (%)
D
PBS
OVA
CD127
GATA3
5.35
11.5
GATA3+ cells (%)
E
Induced
Repressed
T cells
B cells
ILCs
DCs
Myeloid cells
Stromal cells
PP
LP
# of DE genes
Resting CD4+ T
CD8+ T
Activated CD4+ T
γδ T (Xcl1+)
NKT
γδ T (Gzma+)
Resting B
GC B (DZ)
GC B (LZ)
Plasma
ILC3
LTi
NK
ILC1
ILC2
pDC
DC (CD103+ CD11b+)
DC (CD103+ CD11b−)
DC (CD103− CD1)
DC (CD103− CD2)
Macrophage
Mast
Neutrophil
Basophil
Endothelial
Stromal cell (DN)
Fibroblast

Figure 3

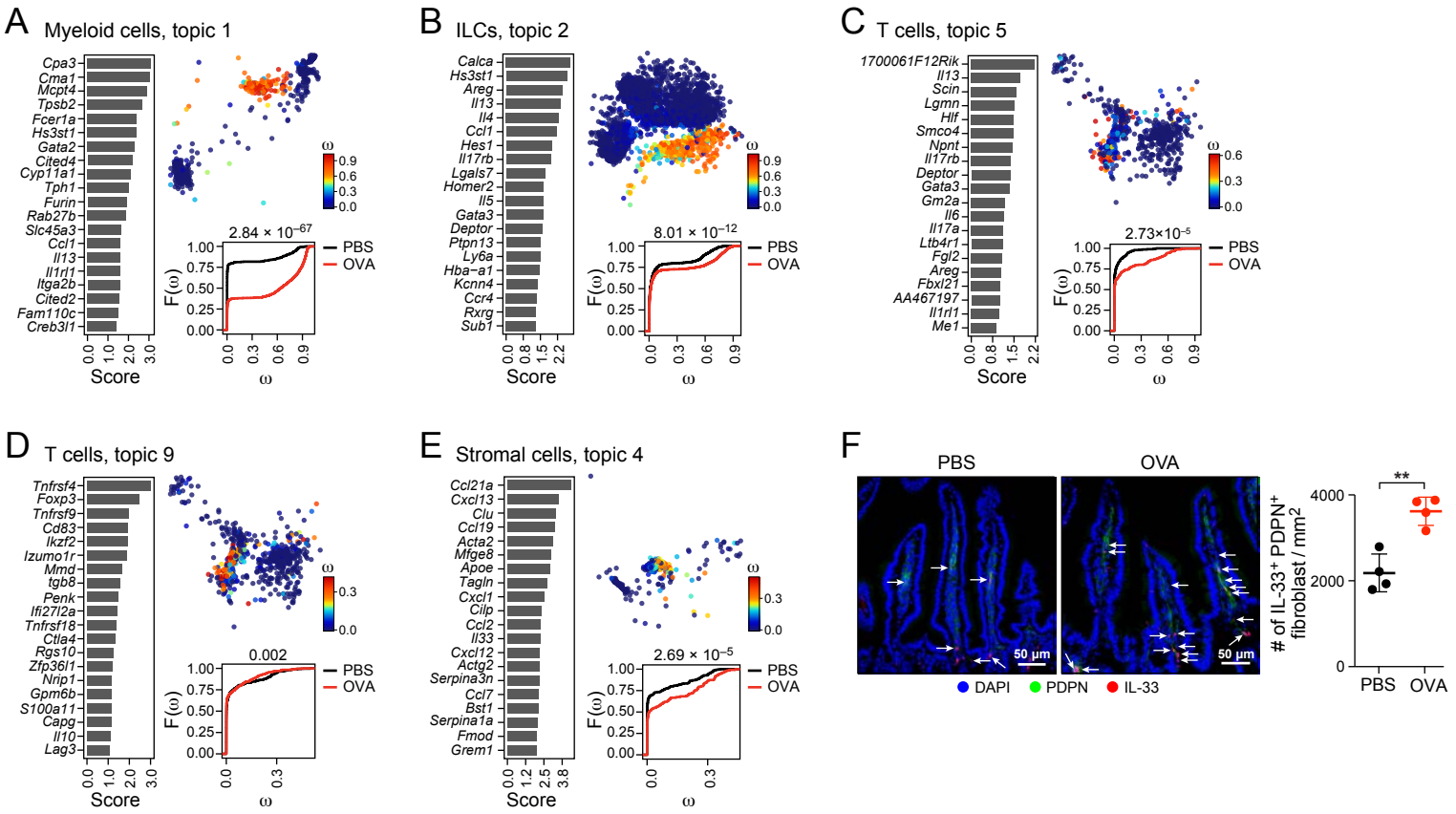
A
Myeloid cells, topic 1
Cpa3
Cma1
Mcpt4
Tpsb2
Fcer1a
Hs3st1
Gata2
Cited4
Cyp11a1
Tph1
Furin
Rab27b
Slc45a3
Ccl1
Il13
Il1rl1
Itga2b
Cited2
Fam110c
Creb3l1
Score
ω
2.84 × 10−67
F(ω)
PBS
OVA
B
ILCs, topic 2
Calca
Hs3st1
Areg
Il13
Il4
Ccl1
Hes1
Il17rb
Lgals7
Homer2
Il5
Gata3
Deptor
Ptpn13
Ly6a
Hba−a1
Kcnn4
Ccr4
Rxrg
Sub1
8.01 × 10−12
C
T cells, topic 5
1700061F12Rik
Il13
Scin
Lgmn
Hlf
Smco4
Npnt
Il17rb
Deptor
Gata3
Gm2a
Il6
Il17a
Ltb4r1
Fgl2
Areg
Fbxl21
AA467197
Il1rl1
Me1
2.73×10−5
D
T cells, topic 9
Tnfrsf4
Foxp3
Tnfrsf9
Cd83
Ikzf2
Izumo1r
Mmd
tgb8
Penk
Ifi27l2a
Tnfrsf18
Ctla4
Rgs10
Zfp36l1
Nrip1
Gpm6b
S100a11
Capg
Il10
Lag3
0.002
E
Stromal cells, topic 4
Ccl21a
Cxcl13
Clu
Ccl19
Acta2
Mfge8
Apoe
Tagln
Cxcl1
Cilp
Ccl2
Il33
Cxcl12
Actg2
Serpina3n
Ccl7
Bst1
Serpina1a
Fmod
Grem1
2.69 × 10−5
F
PBS
OVA
50 μm
DAPI
PDPN
IL-33
# of IL-33+ PDPN+ fibroblast / mm2
4000
2000
0
**

Figure 4

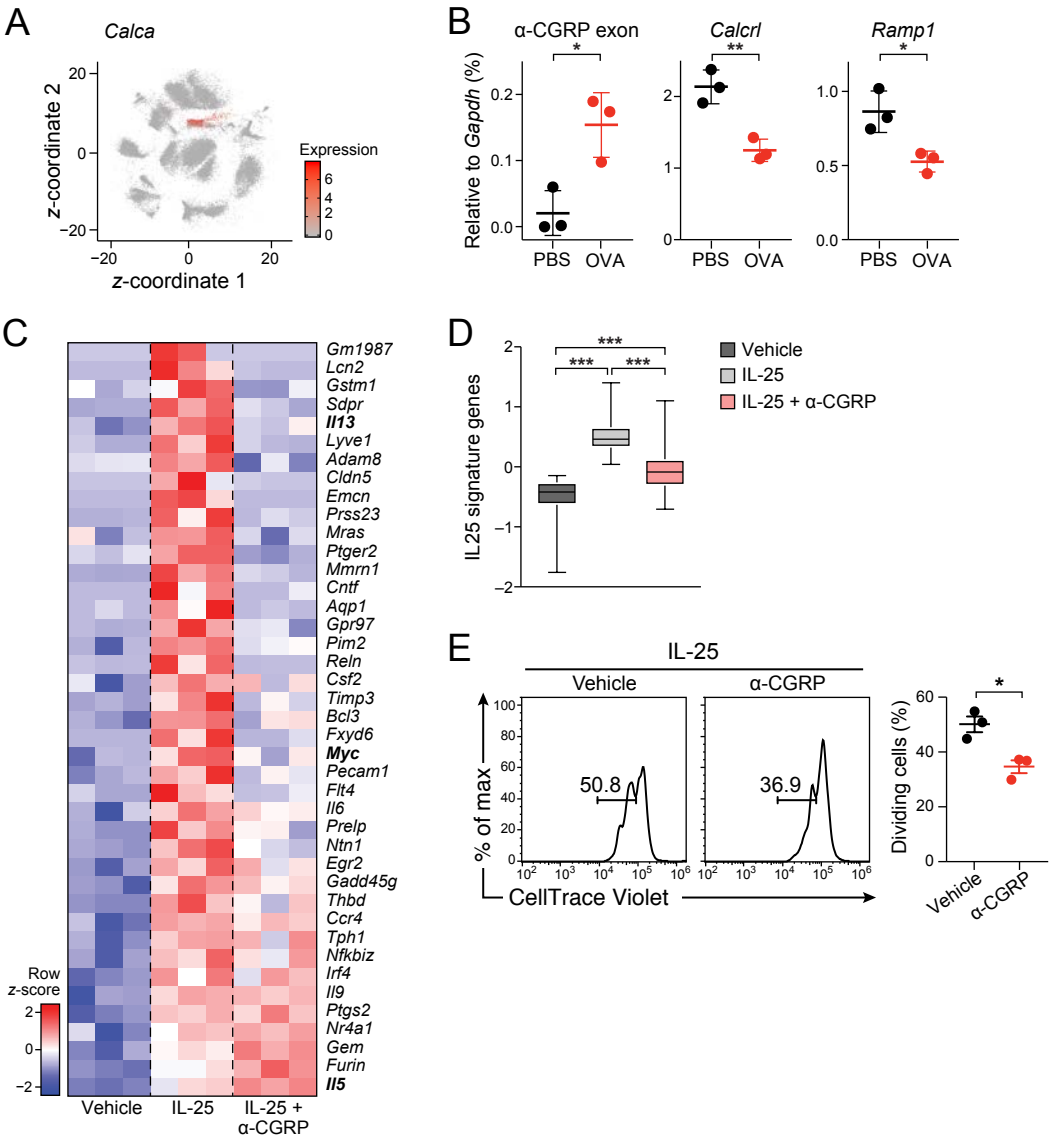
A
Calca
z-coordinate 2
z-coordinate 1
Expression
B
α-CGRP exon
Calcrl
Ramp1
Relative to Gapdh (%)
PBS
OVA
C
Gm1987
Lcn2
Gstm1
Sdpr
Il13
Lyve1
Adam8
Cldn5
Emcn
Prss23
Mras
Ptger2
Mmrn1
Cntf
Aqp1
Gpr97
Pim2
Reln
Csf2
Timp3
Bcl3
Fxyd6
Myc
Pecam1
Flt4
Il6
Prelp
Ntn1
Egr2
Gadd45g
Thbd
Ccr4
Tph1
Nfkbiz
Irf4
Il9
Ptgs2
Nr4a1
Gem
Furin
Il5
Row z-score
Vehicle
IL-25
IL-25 + α-CGRP
D
IL25 signature genes
Vehicle
IL-25
IL-25 + α-CGRP
E
IL-25
Vehicle
α-CGRP
% of max
CellTrace Violet
50.8
36.9
Dividing cells (%)

Figure 5

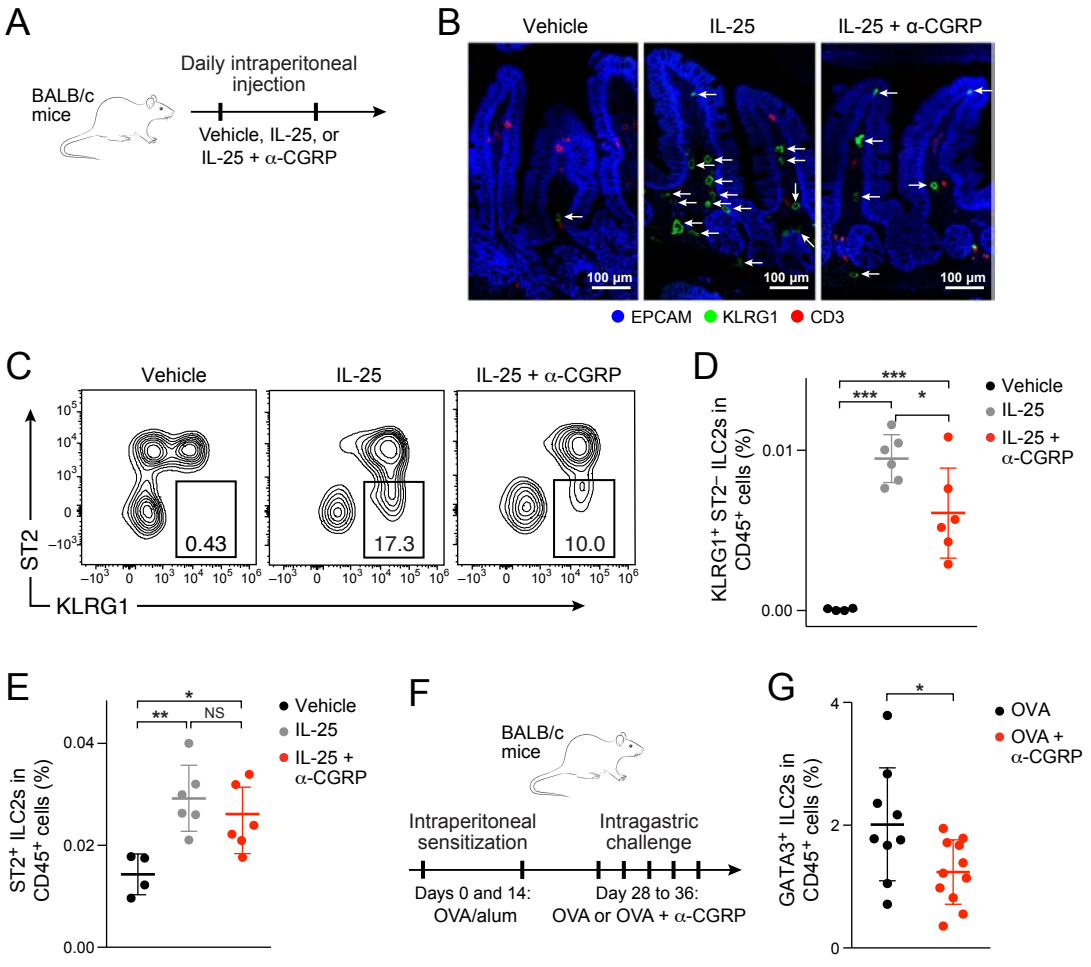
A
BALB/c mice
Daily intraperitoneal injection
Vehicle, IL-25, or IL-25 + α-CGRP
B
Vehicle
IL-25
IL-25 + α-CGRP
100 μm
EPCAM KLRG1 CD3
C
Vehicle
IL-25
IL-25 + α-CGRP
ST2
KLRG1
0.43
17.3
10.0
D
KLRG1+ ST2− ILC2s in CD45+ cells (%)
0.01
0.00
***
***
*
Vehicle
IL-25
IL-25 + α-CGRP
E
ST2+ ILC2s in CD45+ cells (%)
0.04
0.02
0.00
*
**
NS
Vehicle
IL-25
IL-25 + α-CGRP
F
BALB/c mice
Intraperitoneal sensitization
Intragastric challenge
Days 0 and 14: OVA/alum
Day 28 to 36: OVA or OVA + α-CGRP
G
GATA3+ ILC2s in CD45+ cells (%)
4
2
0
*
OVA
OVA + α-CGRP

Figure 6

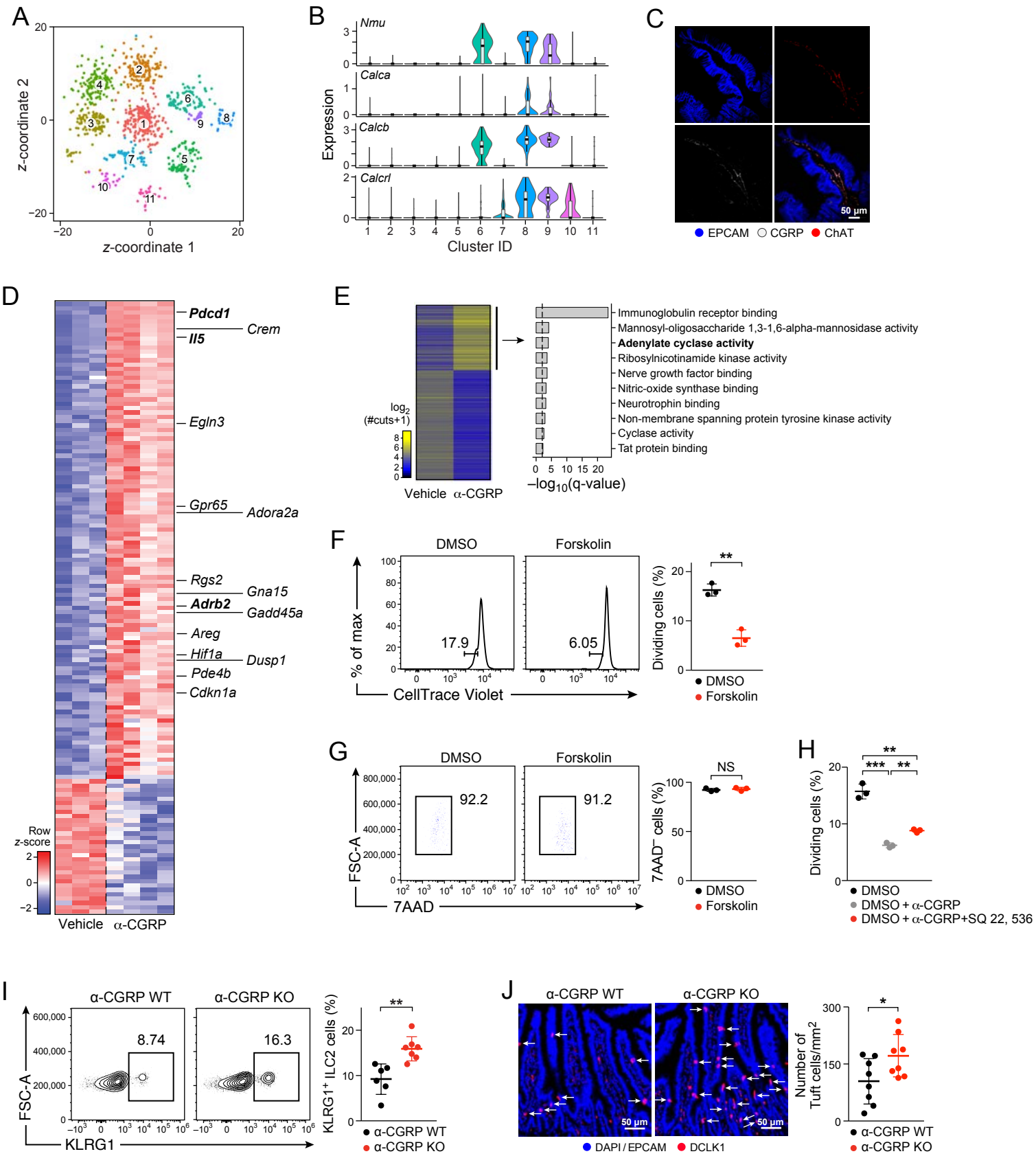
A
z-coordinate 2
z-coordinate 1
B
Nmu
Calca
Calcb
Calcrl
Expression
Cluster ID
C
50 μm
EPCAM CGRP ChAT
D
Pdcd1
Il5
Crem
Egln3
Gpr65
Adora2a
Rgs2
Gna15
Adrb2
Gadd45a
Areg
Hif1a
Dusp1
Pde4b
Cdkn1a
Row z-score
Vehicle α-CGRP
E
log2 (#cuts+1)
Vehicle α-CGRP
Immunoglobulin receptor binding
Mannosyl-oligosaccharide 1,3-1,6-alpha-mannosidase activity
Adenylate cyclase activity
Ribosylnicotinamide kinase activity
Nerve growth factor binding
Nitric-oxide synthase binding
Neurotrophin binding
Non-membrane spanning protein tyrosine kinase activity
Cyclase activity
Tat protein binding
–log10(q-value)
F
DMSO
Forskolin
% of max
17.9
6.05
CellTrace Violet
Dividing cells (%)
DMSO
Forskolin
G
DMSO
Forskolin
92.2
91.2
FSC-A
7AAD
7AAD⁻ cells (%)
NS
DMSO
Forskolin
H
Dividing cells (%)
DMSO
DMSO + α-CGRP
DMSO + α-CGRP+SQ 22, 536
I
α-CGRP WT
α-CGRP KO
8.74
16.3
FSC-A
KLRG1
KLRG1+ ILC2 cells (%)
α-CGRP WT
α-CGRP KO
J
α-CGRP WT
α-CGRP KO
50 μm
DAPI / EPCAM DCLK1
Number of Tuft cells/mm2
α-CGRP WT
α-CGRP KO

Figure 7

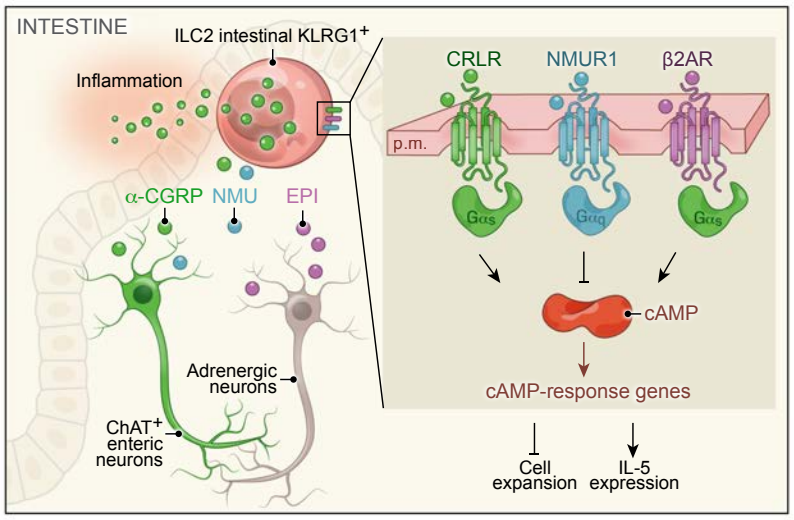
INTESTINE
ILC2 intestinal KLRG1+
Inflammation
α-CGRP
NMU
EPI
Adrenergic neurons
ChAT+ enteric neurons
CRLR
NMUR1
β2AR
p.m.
Gαs
Gαq
Gαs
cAMP
cAMP-response genes
Cell expansion
IL-5 expression

Figure S1

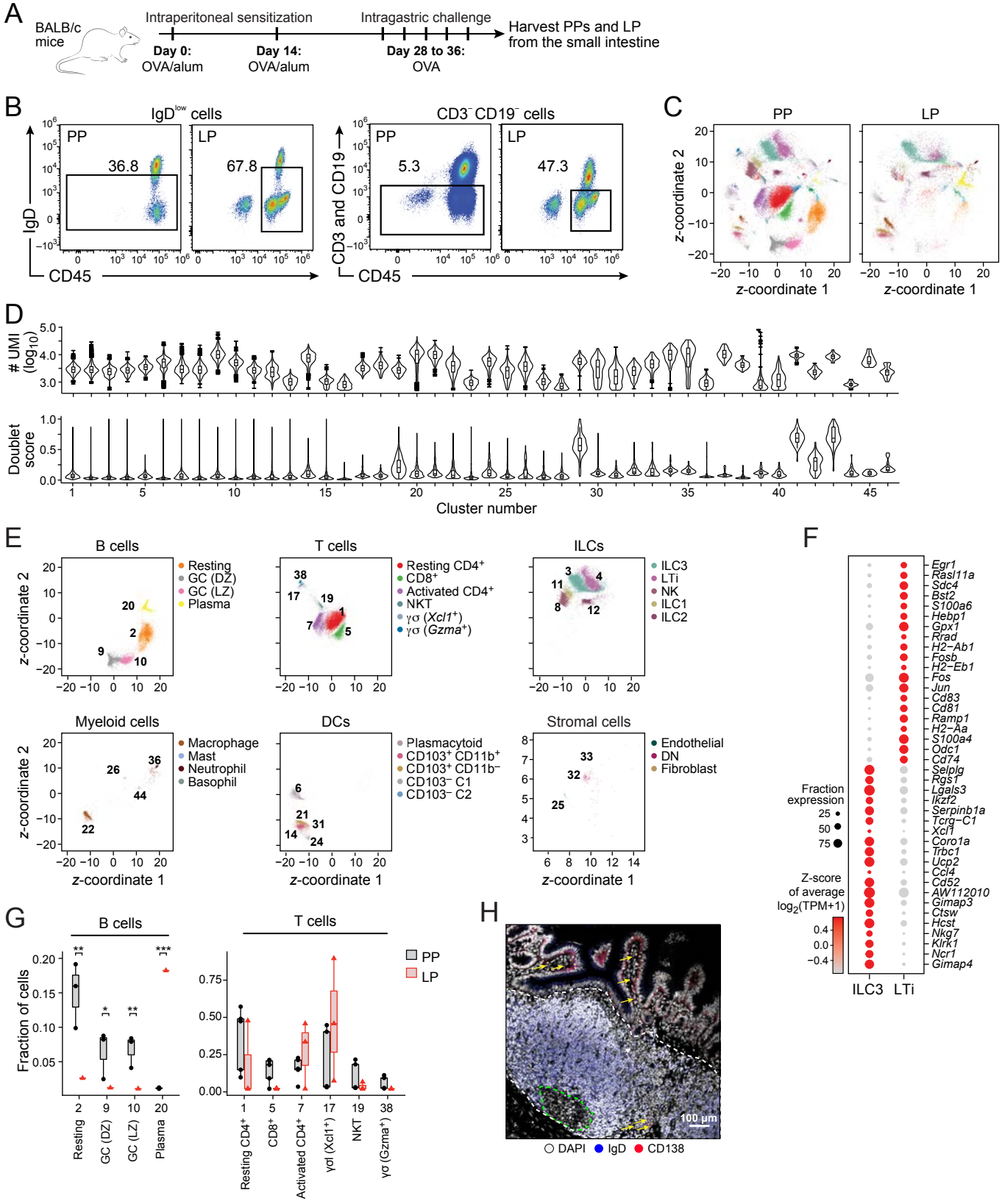
A
BALB/c mice
Intraperitoneal sensitization
Day 0: OVA/alum
Day 14: OVA/alum
Intragastric challenge
Day 28 to 36: OVA
Harvest PPs and LP from the small intestine
B
IgD^low cells
PP
LP
36.8
67.8
IgD
CD45
CD3⁻CD19⁻ cells
5.3
47.3
CD3 and CD19
C
PP
LP
z-coordinate 2
z-coordinate 1
D
UMI (log10)
Doublet score
Cluster number
E
B cells
Resting
GC (DZ)
GC (LZ)
Plasma
T cells
Resting CD4+
CD8+
Activated CD4+
NKT
γσ (Xcl1+)
γσ (Gzma+)
ILCs
ILC3
LTi
NK
ILC1
ILC2
Myeloid cells
Macrophage
Mast
Neutrophil
Basophil
DCs
Plasmacytoid
CD103+ CD11b+
CD103+ CD11b−
CD103− C1
CD103− C2
Stromal cells
Endothelial
DN
Fibroblast
z-coordinate 2
z-coordinate 1
F
Fraction expression
Z-score of average log2(TPM+1)
Egr1
Rasl11a
Sdc4
Bst2
S100a6
Hebp1
Gpx1
Rrad
H2−Ab1
Fosb
H2−Eb1
Fos
Jun
Cd83
Cd81
Ramp1
H2−Aa
S100a4
Odc1
Cd74
Selplg
Rgs1
Lgals3
Ikzf2
Serpinb1a
Tcrg−C1
Xcl1
Coro1a
Trbc1
Ucp2
Ccl4
Cd52
AW112010
Gimap3
Ctsw
Hcst
Nkg7
Klrk1
Ncr1
Gimap4
ILC3
LTi
G
B cells
T cells
PP
LP
Fraction of cells
Resting
GC (DZ)
GC (LZ)
Plasma
Resting CD4+
CD8+
Activated CD4+
γσ (Xcl1+)
NKT
γσ (Gzma+)
H
100 μm
DAPI
IgD
CD138

Figure S2

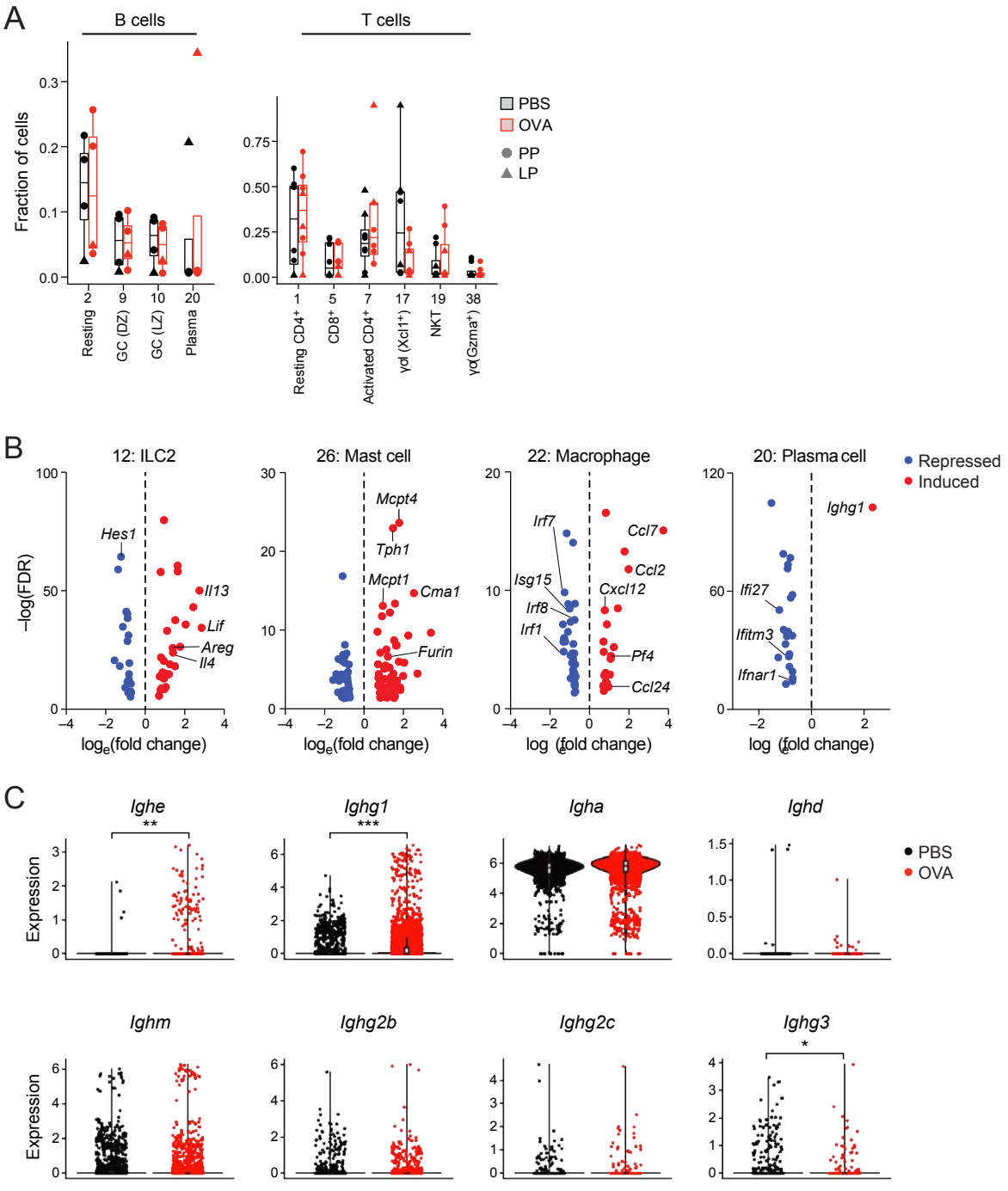
A
B cells
T cells
Fraction of cells
PBS
OVA
PP
LP
Resting
GC (DZ)
GC (LZ)
Plasma
Resting CD4+
CD8+
Activated CD4+
γδ (Xcl1+)
NKT
γδ(Gzma+)
B
12: ILC2
26: Mast cell
22: Macrophage
20: Plasma cell
Repressed
Induced
−log(FDR)
log e(fold change)
Hes1
Il13
Lif
Areg
Il4
Mcpt4
Tph1
Mcpt1
Cma1
Furin
Irf7
Ccl7
Ccl2
Isg15
Cxcl12
Irf8
Irf1
Pf4
Ccl24
Ighg1
Ifi27
Ifitm3
Ifnar1
C
Ighe
Ighg1
Igha
Ighd
Ighm
Ighg2b
Ighg2c
Ighg3
Expression
PBS
OVA

Figure S3

A
Topic 1
Topic 2
Topic 3
Topic 4
Topic 5
Topic 6
Topic 7
Topic 8
Topic 9
Topic 10
Topic 11
Topic 12
Topic 13
Topic 14
Topic 15
Topic 16
tSNE 1
tSNE 2
F(ω)
ω
PBS
OVA
0.05
0.07
1.92×10−6
1.55×10−11
2.73×10−5
3.48×10−14
0.05
8.13×10−23
2.72×10−3
0.23
0.46
0.01
2.26×10−5
3.21×10−15
3.04×10−07
0.01
T cells
B
0.96
0.83
5.00×10−4
3.53×10−11
5.31×10−150
2.71×10−204
1.56×10−73
2.21×10−28
1.55×10−10
4.02×10−65
1.22×10−58
2.2×10−3
9.44×10−154
4.18×10−105
0.08
2.14×10−27
B cells
C
Topic 10
4.84×10−26
8.01×10−12
3.72×10−33
0.78
1.95×10−31
4.45×10−19
1.26×10−55
2.14×10−88
2.04×10−44
0.07
ILCs
D
2.84×10−67
7.91×10−36
5.86×10−59
9.02×10−55
0.142
1.00×10−03
1.87×10−72
2.25×10−67
Myeloid cells
E
2.76×10−15
2.85×10−06
2.10×10−3
7.86×10−24
6.64×10−05
0.90
3.27×10−62
1.72×10−13
2.02×10−101
4.30×10−94
0.90
2.11×10−44
DCs
F
1.73×10−05
0.17
0.14
2.69×10−05
Stromal cells
G
50 μm
DAPI
PDPN
CCL21
IL-33

Figure S4

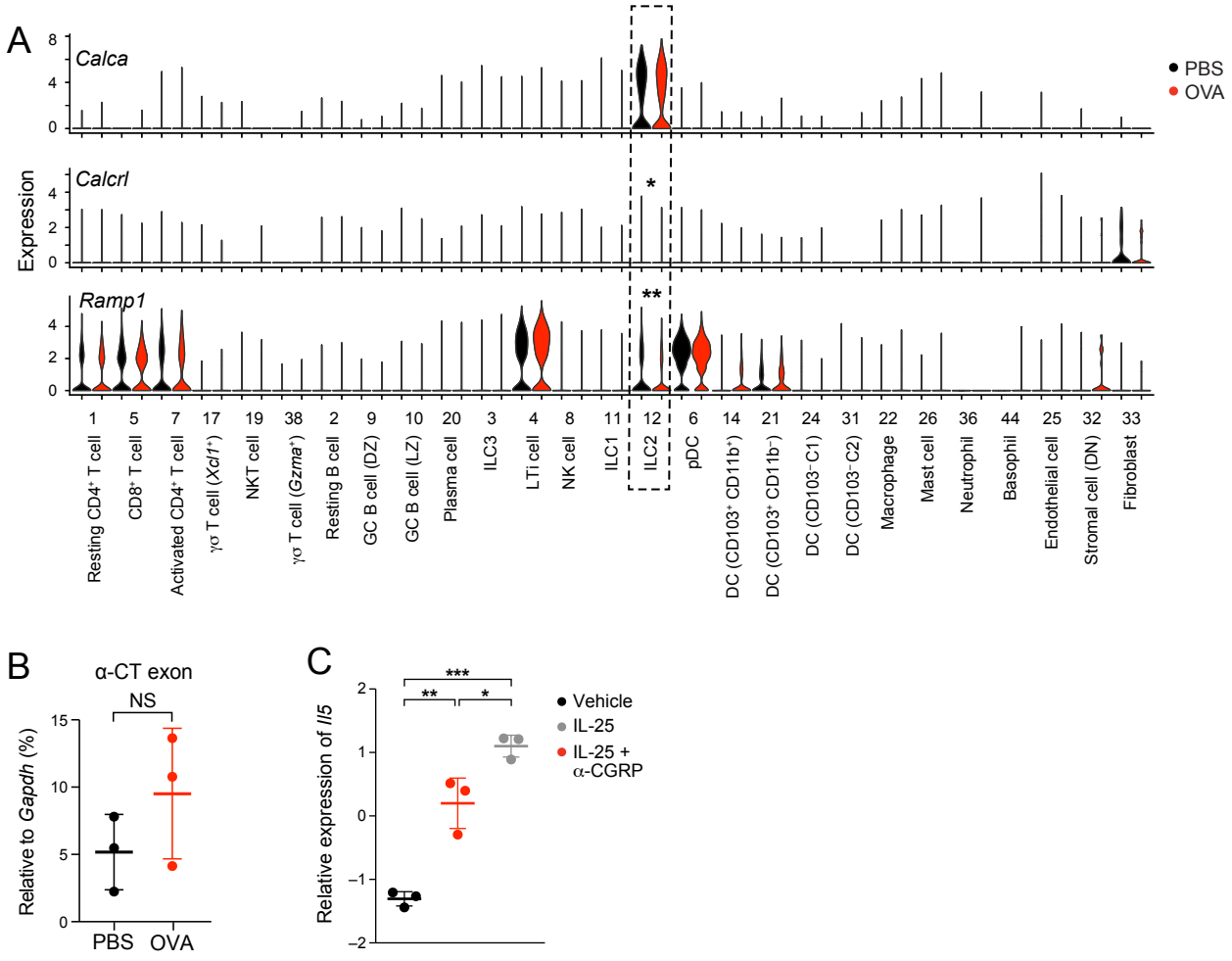
A
Calca
Calcrl
Ramp1
Expression
PBS
OVA
*
**
1 Resting CD4+ T cell
5 CD8+ T cell
7 Activated CD4+ T cell
17 γσ T cell (Xcl1+)
19 NKT cell
38 γσ T cell (Gzma+)
2 Resting B cell
9 GC B cell (DZ)
10 GC B cell (LZ)
20 Plasma cell
3 ILC3
4 LTi cell
8 NK cell
11 ILC1
12 ILC2
6 pDC
14 DC (CD103+ CD11b+)
21 DC (CD103+ CD11b−)
24 DC (CD103− C1)
31 DC (CD103− C2)
22 Macrophage
26 Mast cell
36 Neutrophil
44 Basophil
25 Endothelial cell
32 Stromal cell (DN)
33 Fibroblast
B
α-CT exon
NS
Relative to Gapdh (%)
PBS
OVA
C
***
**
*
Relative expression of Il5
Vehicle
IL-25
IL-25 + α-CGRP

Figure S5

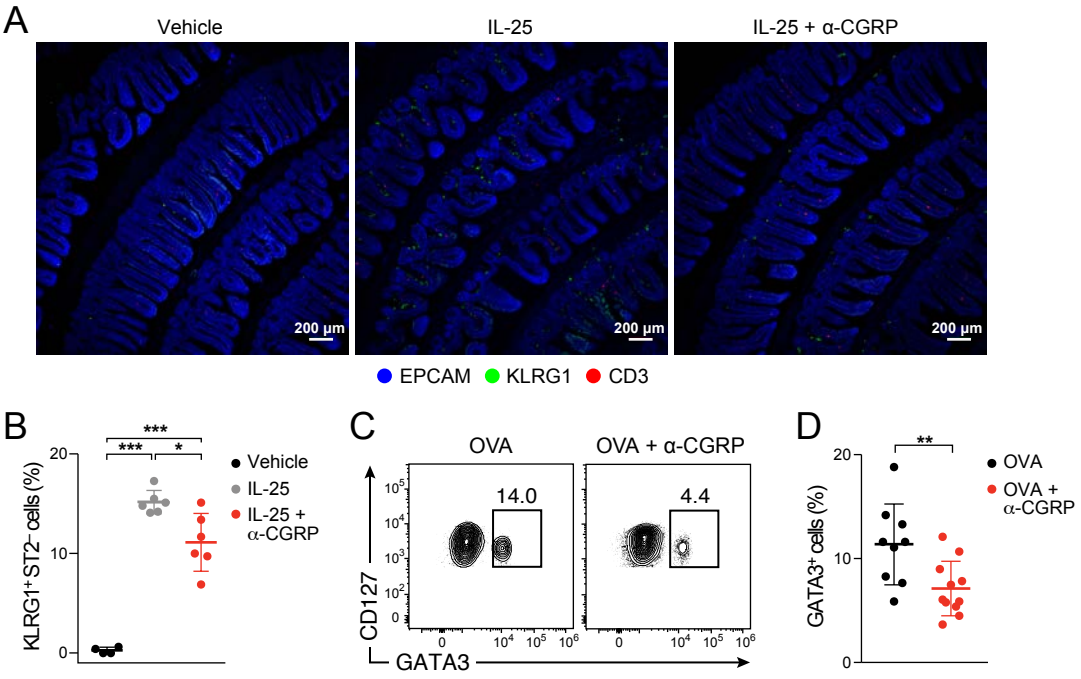
A
Vehicle
IL-25
IL-25 + α-CGRP
200 μm
EPCAM KLRG1 CD3
B
KLRG1+ST2- cells (%)
Vehicle
IL-25
IL-25 + α-CGRP
C
OVA
OVA + α-CGRP
14.0
4.4
CD127
GATA3
D
GATA3+ cells (%)
OVA
OVA + α-CGRP

Figure S6

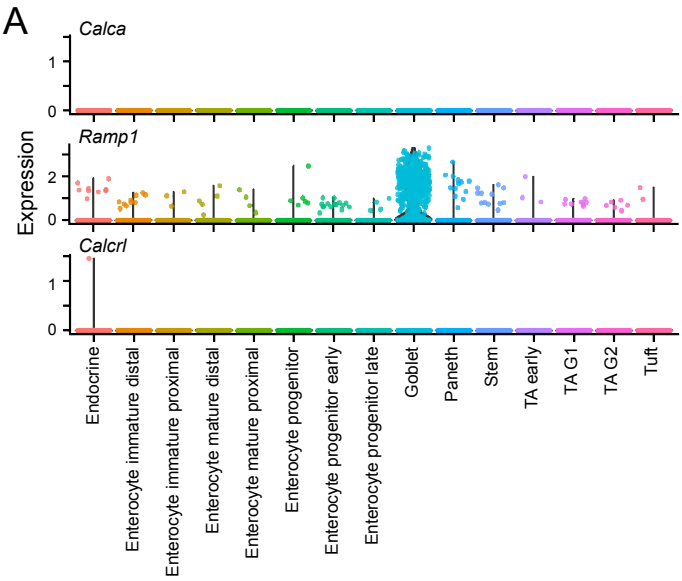
A
Calca
Ramp1
Calcrl
Expression
Endocrine
Enterocyte immature distal
Enterocyte immature proximal
Enterocyte mature distal
Enterocyte mature proximal
Enterocyte progenitor
Enterocyte progenitor early
Enterocyte progenitor late
Goblet
Paneth
Stem
TA early
TA G1
TA G2
Tuft

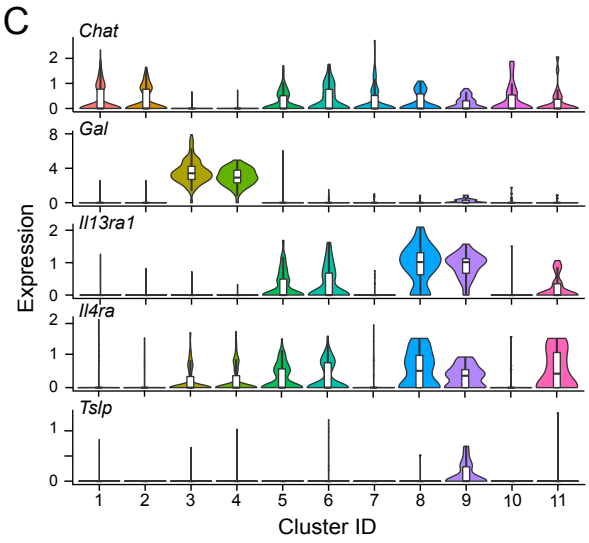
C
Chat
Gal
Il13ra1
Il4ra
Tslp
Expression
Cluster ID

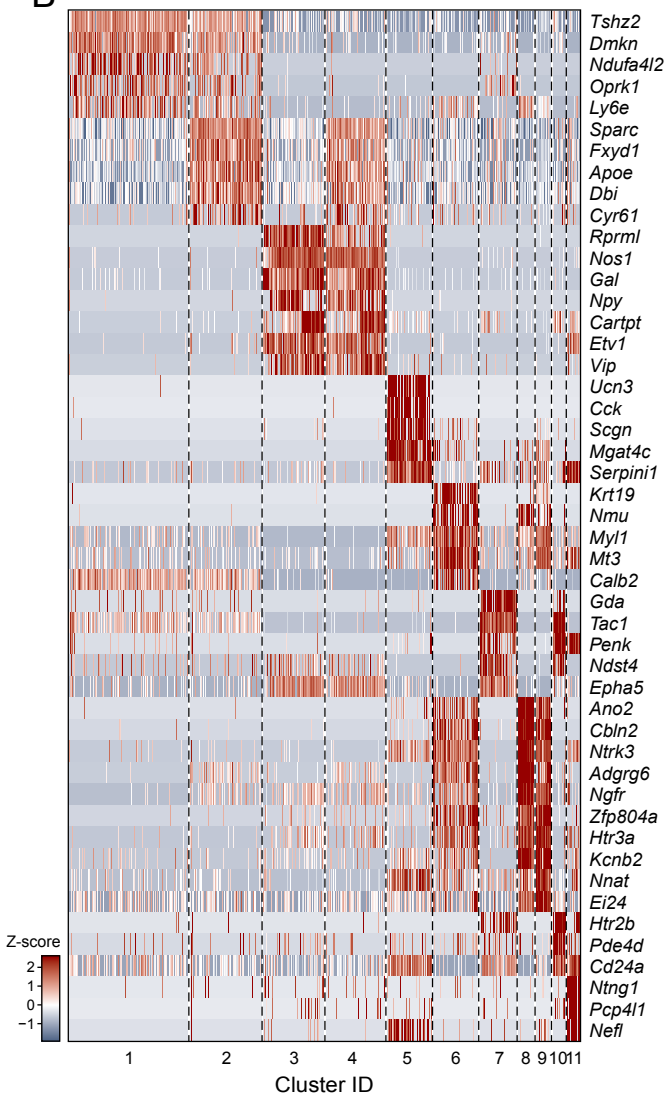
B
Tshz2
Dmkn
Ndufa4l2
Oprk1
Ly6e
Sparc
Fxyd1
Apoe
Dbi
Cyr61
Rprml
Nos1
Gal
Npy
Cartpt
Etv1
Vip
Ucn3
Cck
Scgn
Mgat4c
Serpini1
Krt19
Nmu
Myl1
Mt3
Calb2
Gda
Tac1
Penk
Ndst4
Epha5
Ano2
Cbln2
Ntrk3
Adgrg6
Ngfr
Zfp804a
Htr3a
Kcnb2
Nnat
Ei24
Htr2b
Pde4d
Cd24a
Ntng1
Pcp4l1
Nefl
Z-score
Cluster ID

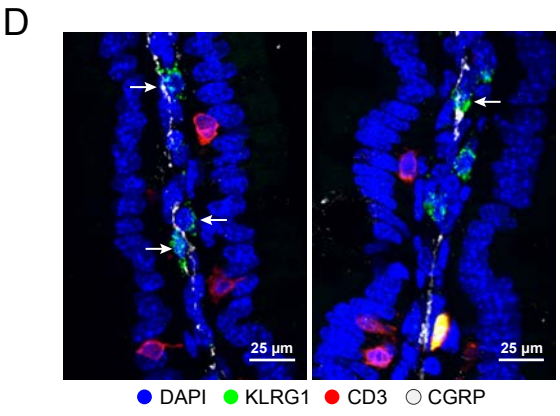
D
25 µm
25 µm
DAPI
KLRG1
CD3
CGRP

Supplemental Table 1

Supplemental Table 2

Supplemental Table 3

Click here to access/download

Supplemental Videos and Spreadsheets

Xu et al table S3.xlsx

Supplemental Table 4

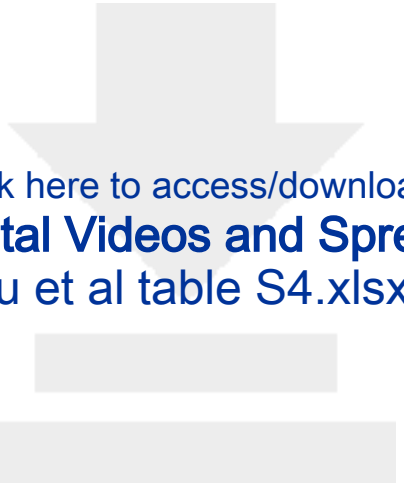

Click here to access/download

Supplemental Videos and Spreadsheets

Xu et al table S4.xlsx

Supplemental Table 5

Click here to access/download

Supplemental Videos and Spreadsheets

Xu et al table S5.xlsx